

1 **Perinatal brain group 3 innate lymphoid cells are involved in the formation of**
2 **murine dural lymphatics**

3
4 Alba del Rio Serrato^{1,2,3,4}, Borja Latorre Hernández^{1,2,3,4}, Evie Bartl^{1,2,3}, Christina Stehle^{5,6},
5 Oliver Hölsken^{7,8,9,10}, Andreas Diefenbach^{7,8}, Chiara Romagnani^{5,6}, Carmen Infante-
6 Duarte^{1,2,3,4*}

7
8 ¹ECRC Experimental and Clinical Research Center, a Joint Cooperation between the Charité-
9 Universitätsmedizin Berlin and Max-Delbrück-Center for Molecular Medicine, 13125 Berlin,
10 Germany

11 ²Charité – Universitätsmedizin Berlin, corporate member of Freie Universität Berlin and
12 Humboldt Universität zu Berlin, ECRC Experimental and Clinical Research Center,
13 Lindenberger Weg 80, 13125 Berlin, Germany

14 ³Max-Delbrück-Center for Molecular Medicine in the Helmholtz Association (MDC), 13125
15 Berlin, Germany

16 ⁴Berlin Institute of Health at Charité – Universitätsmedizin Berlin, Charitéplatz 1, 10117
17 Berlin, Germany

18 ⁵Innate Immunity, Deutsches Rheuma-Forschungszentrum Berlin (DRFZ), ein Leibniz Institut,
19 Berlin, Germany

20 ⁶Charité – Universitätsmedizin Berlin, corporate member of Freie Universität Berlin and
21 Humboldt Universität zu Berlin, Institute of Medical Immunology (I-MI), Augustenburger Platz
22 1, 13353 Berlin, Germany

23 ⁷Charité – Universitätsmedizin Berlin, corporate member of Freie Universität Berlin and
24 Humboldt Universität zu Berlin, Institute of Microbiology, Infectious Diseases and Immunology
25 (I-MIDI), Hindenburgdamm 30, 12203 Berlin, Germany

26 ⁸Mucosal and Developmental Immunology, Deutsches Rheuma-Forschungszentrum (DRFZ),
27 an Institute of the Leibniz Association, Berlin, Germany

28 ⁹Charité – Universitätsmedizin Berlin, corporate member of Freie Universität Berlin and
29 Humboldt Universität zu Berlin, Department of Anesthesiology and Intensive Care Medicine,
30 Hindenburgdamm 30, 12203 Berlin, Germany

31 ¹⁰Berlin Institute of Health at Charité – Universitätsmedizin Berlin, BIH Academy, Clinician
32 Scientist Program, Charitéplatz 1, 10117 Berlin, Germany

33
34 **Corresponding author:** Carmen Infante-Duarte, Experimental and Clinical Research Center,
35 Charité Universitätsmedizin Berlin and Max Delbrück Center for Molecular Medicine (MDC),
36 Berlin, Germany. Lindenberger Weg 80, 13125, Berlin. Phone: +4930450540298;
37 carmen.infante@charite.de

38 **Summary**

39 The central nervous system (CNS) contains a pool of innate lymphoid cells (ILCs) of unclear
40 composition and functionality and unknown origin. Here, we demonstrate that group 1 ILCs
41 (inc. ex-ILC3s) and ILC2s are resident cells with low proliferative capacities and subtype
42 specific CNS compartmentalization. We show for the first time that CNS ILC seeding and niche
43 establishment occurs during early life and is initiated by both, ILC progenitors-like PLFZ⁺PD-
44 1⁺ cells and lineage committed ILCs. While group 1 ILCs and RORγt⁺ ILC3s were found within
45 the embryonic and postnatal brain, ILC2s reached the CNS after birth and were predominantly
46 localized within the dura mater, proving early regional distribution. Interestingly, RORγt⁺ ILC3s
47 were only detected perinatally and vanished from the CNS as an outcome of decreased
48 turnover and *in situ* ILC3-to-ILC1 conversion. Remarkably, we showed that perinatal RORγt⁺
49 ILC3s are required for the correct development of the lymphatic vessels within the dura.

50

51 Keywords: Innate lymphoid cells, central nervous system, tissue resident lymphocytes,
52 embryonal development, ILC seeding, ILC3s, ILC plasticity, cellular turnover, dura lymphatic
53 vessels

54

55 **Introduction**

56 Innate lymphoid cells (ILCs) form a heterogeneous group of tissue resident innate immune
57 cells that act not only as key modulators of the immune response but are also involved in other
58 processes such as tissue homeostasis, repair, and remodeling¹⁻⁴. ILCs are categorized in five
59 subsets based on their developmental pathways and phenotypical profiles. Group 1 ILCs
60 includes conventional natural killer (NK) cells, that express the transcription factor (TF)
61 eomesodermin (Eomes)⁵, and helper ILC1s. Both subsets express T-bet⁵ and produce large
62 amounts of IFN-γ^{6,7}. Group 2, characterized by high expression of GATA-3, produce
63 amphiregulin, IL-4, IL-5, or IL-13 and are enriched in barrier structures such as the skin, lung,
64 and intestine. Finally, RORγt-dependent group 3 ILCs, including NKp46^{+/-} ILC3s and CCR6⁺
65 lymphoid tissue inducer (LTi) cells, are characterized by the production of lymphotoxin-α, IL-
66 17 and IL-22.

67 ILCs develop from the common lymphoid progenitor (CLP) and appear to seed tissues already
68 at prenatal stages, displaying organ-specific distribution and composition^{8,9}. The main
69 hematopoietic ILC sources are the fetal liver and the adult bone marrow; however, circulating
70 fetal ILC progenitors that seed peripheral tissues and undergo *in situ* differentiation have also
71 been observed¹⁰⁻¹². Indeed, parabiotic experiments confirmed that the ILC pool in many
72 tissues is comprised by both embryonic-derived long-lived cells and a fraction that is
73 generated during adulthood¹³⁻¹⁶. Additionally, plasticity events mediated by e.g. tissue-derived
74 cytokines have been reported within all ILC subsets^{17,18}, leading to the generation of a plethora

75 of intermediate populations¹⁹⁻²². Overall, these processes of layered ontogeny, adult-derived
76 turnover, and ILC plasticity, facilitate the adaptation of tissue-specific ILCs to external stimuli
77 during immune activation and physiological processes of tissue development, homeostasis
78 and aging^{12,23,24}.

79 ILCs have been mainly described in barrier structures such as the airways, digestive tract, and
80 skin; though, we and others have reported on resident ILCs within the central nervous system
81 (CNS)^{6,25-27}. Most of these studies focused on the ILC distribution and function in inflamed
82 CNS compartments. Within the meningeal barriers, ILCs modulate T cell activation and
83 trafficking during autoimmune neuroinflammation by acting as antigen-presenting cells^{28,29},
84 tissue healing after spinal cord injury³⁰, and sex-dimorphism in the T cell response during
85 experimental autoimmune encephalomyelitis (EAE)³¹. However, because of the low ILC
86 numbers in the steady-state CNS, little is known on dynamics of tissue seeding, local
87 differentiation, and their possible roles in CNS homeostasis and development.

88 Here, we demonstrated that group 1 and ILC2s are quiescent CNS resident cells with low
89 proliferative capacities and compartment-specific distribution. Importantly, we defined the
90 formation of the CNS-ILC niche during embryonic development and postnatal stages. While
91 group 1 ILCs, ROR γ ⁺ ILC3s, and LTi cells were detected in the brain prenatally, ILC2s mainly
92 reached the brain after birth. Further, the ILC distribution along the different CNS
93 compartments is already established after the second week of life. ROR γ ⁺ ILC3s, transiently
94 appeared during perinatal stages of brain development but are absent in the adult CNS due
95 to, in part, postnatal *in situ* ILC3 to ILC1 conversion. Ex-ILC3s appeared as a population with
96 long-lived capacities as a proportion of these cells remained in the brain until, at least, 7
97 months of age. Remarkably, we showed that the presence of perinatal ROR γ ⁺ ILC3s is
98 required for the correct development of the lymphatic vessels within the dura mater.

99

100 **Results**

101

102 **Group 1 ILCs (including ex-ILC3s) and ILC2s but not ILC3s are tissue-resident immune** 103 **cells in the young adult CNS**

104 To determine the ILC profile of the murine adult CNS, we performed high-dimensional flow
105 cytometry and identified group 1 ILCs and ILC2s as main ILC populations within the tissue
106 (Representative gating strategy is shown in Fig. 1A; Sup. Fig. 1A). To confirm these results,
107 we examined an available scRNA-seq dataset of the whole murine brain and brain barrier-
108 sorted immune cells³². Group 1 and 2 ILCs were identified as the sole ILC populations along
109 the different CNS compartments (Fig. 1B), after excluding clusters with markers for other
110 immune cell populations and selecting those clusters with the highest ILC signature score
111 (Sup. Fig. 1B-D; ILC signature genes depicted in Sup. Table 1).

112 Confirming our and others' previous work^{6,33}, CNS group 1 ILCs, expressing NK1.1, NKp46
113 and CD122 (IL-2R β), conveyed not only conventional Tbet⁺Eomes⁺ NK cells but also Eomes⁻
114 ILC1s that were highly positive for CD90.2 and showed intermediate levels of CD200R
115 expression (Fig. 1A, C; Sup. Fig. 1E). Mature ILC2s were identified by the expression of
116 CD127, CD90.2, ST2 (IL-33R), and CD25 (IL-2R α), together with high expression of CD200R
117 (Fig. 1C). No significant differences were observed between female and male young CNS in
118 terms of the proportion and absolute number of total ILCs or ILC subsets (Fig. 1D, E; Sup. Fig.
119 2A, B).

120 We found ILCs along all investigated CNS regions, i.e., brain parenchyma (including
121 leptomeninges) (B.P, 348.2 \pm 46.99), choroid plexus (Ch.P, 222.7 \pm 36.8), and dura mater
122 (D.M, 964.6 \pm 114.9), but not in spinal cord parenchyma (SC.P, 3.32 \pm 0.64), which was
123 therefore excluded from subsequent experiments (Fig. 1E, F). In contrast to peripheral blood,
124 ILC2s were the main population detected in the dura mater, whereas group 1 ILCs (both ILC1s
125 and NK cells) were more prevalent in the brain parenchyma and choroid plexus (Fig. 1G, H).
126 Strikingly, we observed negligible amounts of ILC3s in all CNS compartments (Fig. 1G, H).
127 CNS ILCs displayed a low proliferative capacity (Fig. 1I, Sup. Fig. 1F). Within the brain
128 parenchyma, all ILC subsets showed proliferation rates below 20% (Fig. 1I) in both female
129 and male animals (Sup. Fig. 2C), while a slightly higher proliferation rate was observed for
130 group 1 ILCs in dura and choroid plexus (Fig. 1I). Furthermore, transcript analysis showed low
131 levels of cytokine expression among the different ILC clusters, especially among ILC2s, further
132 indicating low basal activity of ILCs in the steady-state CNS (Sup. Fig. 1F). Intravenous
133 injections of anti-CD45-PE 3 min prior to euthanasia and perfusion, further demonstrated that
134 the investigated populations excluded blood contaminant cells, identified as CD45-PE⁺ cells
135 (Sup. Fig. 1G). Up to 90-99% of the tissue-resident helper-like ILCs were CD45-negative (Fig.
136 1J). In contrast, within the B.P and D.M, the NK cell fraction encompassed 25-35% of cells
137 derived from the blood circulation or associated with the brain vasculature (Fig. 1J). In fact,
138 scRNA-seq data also showed both; the helper-like clusters and the majority of NK cells
139 presenting a tissue-resident signature (*Cd69*, *Rgs1* or *Il1rl1* for ILC2s) and a fraction of NK
140 cells showing higher expression of genes associated with a circulating phenotype (*Sell*, *S1pr1*
141 and *Klf2*) (Sup. Fig. 1H). Helper-like ILCs were enriched in homing receptor *Cxcr6*, while *Ccr5*
142 was predominantly present among NK cells and ILC1s. Interestingly, *Ccr2* was highly
143 expressed among all ILC subsets (Sup. Fig. 1I).

144 Thus far, our data show that resting and quiescent tissue-resident ILCs are present within the
145 adult CNS. While group 1 ILCs and ILC2s are enriched in the B.P and Ch.P, ILC2s are the
146 main population in the D.M. Furthermore, although we had previously reported on the
147 presence of ex-ILC3s within the steady-state CNS⁶, no ILC3s were observed along adult CNS

148 structures. To complement our previous data, we used fate map
149 *Rorc(gt)^{cre} × R26R^{eYFP}* (ROR γ t-FM) mice and analyzed the presence of ex-ILC3s in 2-3-month-
150 old mice. Using this reporter line, we confirmed the absence of ILC3s and the presence of ex-
151 ILC3s principally among T-bet⁺ ILCs (Fig. 1K) and, in a much lesser extent, among T-bet⁺ST2⁺
152 ILCs (Sup. Fig. 1J) in adult mice. This data suggests an early presence of ROR γ t⁺ ILC3s within
153 the CNS. T-bet⁺ ex-ILC3s expressed CD122 and NK1.1, and appeared predominantly within
154 the whole brain ($18.4 \pm 3.5\%$ within T-bet⁺ cells), while T-bet⁺ST2⁺ ex-ILC3s accounted for less
155 than a 5% of the dura and brain ST2⁺ ILC2s (Sup. Fig. 1J).

156

157 **ILCs start infiltrating the brain prenatally as progenitor-like cells and mature ILCs**

158 To investigate whether the presence of ex-ILC3s in the adult brain truly reflects the existence
159 of ROR γ t⁺ ILC3s in earlier developmental stages, we focused on deciphering the dynamics of
160 ILC seeding and niche establishment within the whole brain (excluding dura meninges) along
161 ontogeny.

162 First, we investigated the presence of ILCs within the prenatal brain using Id2^{GFP/+} reporter
163 mice, which is expressed in all ILCs. We could confirm that the expression pattern CD45^{high}
164 Lineage⁻LD⁻CD3⁻CD122⁺ and/or CD127⁺ defines *bona fide* CNS Id2-GFP⁺ ILCs at the
165 embryonic stage (Fig. 2A). Brain ILCs were nearly absent at E14 (Id2⁺CD122⁺: $4.43 \pm 1.18\%$;
166 Id2⁺CD127⁺: $2.16 \pm 1.11\%$) but appeared clearly enriched at E16 (Id2⁺CD122⁺: $16.55 \pm 5.39\%$;
167 Id2⁺CD127⁺: $12.7 \pm 5.24\%$) (Fig. 2B), positioning the beginning of the ILC seeding into the
168 CNS between these two timepoints. Notably, we were able to identify CD122⁺CD127⁻ (P1),
169 CD122⁻CD127⁺ (P3), and double-positive CD122⁺CD127⁺ (P2) cells (Fig. 2A), which lack CD5
170 and express other ILC markers such as CD90.2, CXCR3 (in the case of CD122-expressing
171 cells) and CXCR6 (Fig. 2A, C). Although CD127⁺ cells (P2 and P3) express markers such as
172 integrin $\alpha 4\beta 7$ and c-Kit, they lack expression of CD135 (Flt3), excluding the presence of CLPs
173 (live CD45⁺Lineage⁻CD3⁻CD5⁻CD127⁺ $\alpha 4\beta 7^{+/-}$ cKit⁺CD135⁺). Nevertheless, we identified
174 PLZF^{high}PD-1⁺ ILC progenitor-like cells among total *bona fide* CNS ILCs, especially enriched
175 in the CD122⁺CD127⁺ (P2) population (ILC progenitor-like cells brain: $16.45 \pm 11.7\%$) (Fig.
176 2D). These PLZF^{high}PD-1⁺ ILC progenitor-like cells showed high expression of Gata3 (without
177 expressing the ILC2-marker IL2 α (CD25), data not shown) and showed intermediate levels
178 of ROR γ t and T-bet (Fig. 2E), which generally characterize ILC progenitors that are still able
179 to differentiate into distinct ILC subsets³⁴. In parallel, high and mutually exclusive expression
180 of lineage-associated TFs (i.e. high T-bet-expression in CD127⁻CD122⁺ cells, enriched in
181 group 1 ILCs) was also observed at this timepoint, indicating the co-existence of differentiated
182 and committed ILCs among this first wave of embryonal ILC infiltration (Fig. 2E).

183

184 **Brain ILC seeding occurs in a subset-specific manner**

185 Next, we investigated the seeding kinetics of lineage-committed ILCs during the pre- and
186 postnatal stages starting at the identified timepoint of initial infiltration (E16). We defined
187 $CD45^{high}LinLD^{-}CD3^{-}CD122^{+}$ and/or $CD127^{+}$ cells as total ILCs and confirmed along ontogeny
188 that the $Id2^{-}CD122^{-}CD127^{-}$ population did not contain ROR γ t, T-bet, or Gata3-expressing cells
189 (Fig. 3A). Interestingly, ILCs infiltrated the brain earlier than adaptive T lymphocytes
190 ($CD45^{high}LinLD^{-}CD3^{+}$), which were first detectable after birth (Fig. 3B). Furthermore, the
191 calculation of ILCs per gram of brain showed that ILC numbers increased with brain weight,
192 maintaining the ILC prevalence throughout the neonatal period and young adult life (Fig. 3C).
193 Using ROR γ t, T-bet, or Gata3 to identify the different ILC subsets (Fig. 3A), we observed
194 lineage-specific kinetics of brain seeding during development (Fig. 3D, E). $CD122^{+}T-bet^{+}$
195 group 1 ILCs was the largest population across all developmental timepoints, both in
196 percentage and absolute numbers (Fig. 3D, E). Both Eomes $^{+}$ and Eomes $^{-}$ cells were identified
197 pre- and postnatally (Sup. Fig. 3A). Until P1, Eomes $^{-}$ cells appeared more predominant in
198 frequency and absolute numbers (Sup. Fig. 3B, C), but their proportion decreased to 20-40%
199 after the first week of life as the absolute numbers of Eomes $^{+}$ cells increased (Sup. Fig. 3B,
200 C). The increase in the Eomes $^{+}$ population appeared to be caused by an influx of peripheral
201 cells, as the proliferation rates of Eomes $^{-}$ and Eomes $^{+}$ cells were generally comparable (Sup.
202 Fig. 3D). On the other hand, the second major population observed in the adult brain,
203 Gata3 $^{+}CD90.2^{+}$ ILC2s (ST2 $^{+}$, data not shown), appeared to start infiltrating the brain after birth,
204 with increased prevalence and absolute numbers between P9 and 5w (Fig. 3D, E). Finally, we
205 confirmed that ROR γ t-expressing cells were transiently present perinatally, starting at very
206 low levels at E16 but peaking by P9 (78.06 ± 21.9 cells/animal). Subsequently, their numbers
207 started decreasing (P15: 35.2 ± 8.2 cells/animal; 5w: 53.07 ± 10.09 cells/animal) until almost
208 complete retraction was observed in 10-week-old animals (Fig. 1A, G, H; Fig. 3D, E). Parallel
209 analysis of peripheral blood ILCs along ontogeny showed differences in the prevalence of
210 circulating ILC subtypes, indicating different waves of ILC mobilization (Fig. 3E, F). In this line,
211 we observed a high proliferative capacity of all brain ILC subsets between E16 and P1 (Fig.
212 3G), which decreased progressively at later timepoints (Fig. 3G). Interestingly, as the
213 proliferative capacity of embryonal CNS ILCs decreased at P9, the numbers in group 1 ILCs
214 and ILC2s increased appreciably in the brain and peripheral blood circulation (Fig. 3E, F).
215 Thus, we concluded here that a first wave of embryonal CNS ILC seeding combined with high
216 levels of *in situ* proliferation drives the initial formation of the prenatal CNS ILC pool. However,
217 the second wave of infiltrating ILCs during the first two weeks of life accounted for the further
218 expansion of the brain ILC pool and the establishment of the ILC profile observed in the young
219 adult CNS.

220 Altogether, we showed for the first time that ILCs start infiltrating the brain prenatally, earlier
221 than adaptive T lymphocytes, in the form of both uncommitted PLZF⁺PD-1⁺ ILC progenitor-
222 like cells and lineage-committed ILC1s, ILC2s, and, as hypothesized, ILC3s. Moreover, our
223 data indicate that the formation of the CNS ILC pool is supported by a first wave of ILC
224 infiltration followed by perinatal *in situ* proliferation and differentiation, whereas a second wave
225 of infiltrating ILCs further expands the ILC pool after the first week of life.

226

227 **scRNA-seq analysis of postnatal ILCs reveals a mature ILC compartment with presence** 228 **of group 3 ILCs**

229 Analysis of ROR γ t-FM mice at different postnatal ages confirmed that ILC3s were present
230 predominantly in the developing brain and peaked at P9 (Fig. 4A). To explore the properties
231 of ILCs within the newborn CNS, we performed scRNA-seq analysis of CD45⁺LinLD⁻CD3⁻CD5⁻
232 CD122⁺/CD127⁺ ILCs from the whole brain and dura mater of P9.5 mice, as depicted in Figure
233 4B. This first-reported single-cell analysis of CNS ILCs was conducted with 480 cells from the
234 brain and 362 cells from the dura mater after quality control and cell selection. We identified 5
235 distinct clusters of *Id2*-expressing cells with transcripts for *Gata3*, *Tbx21*, *Rorc*, and *Eomes*,
236 as well as different associated ILC signature markers among their top differentially expressed
237 genes (DEGs). ILC2s, cluster 0, expressing *Gata3*, *Il1r1*, *Icos*, *Csf2*; ILC1s, cluster 1,
238 expressing *Tbx21*, *Cd7*, *Ncr1*, *Nkg7*, *Il2rb*, and *Xcl1*; ILC3s, cluster 2, expressing *Rorc*, *Cxcr5*,
239 *Cd4*, *Tcf7*, *Nrgn*, and *Lta*; and some NK cells, cluster 3, expressing *Tbx21*, *Eomes*, *Ccr5*, *Ccl5*,
240 *Gmza*, and *Sell*. Cluster 4 represented a mixture of the previous clusters with additional
241 markers for cell proliferation, such as *Mki67*, *Tuba1b*, and *Tubb5* (Fig. 4C, D; Sup. Fig 4A).
242 Cells clustered based on ILC-subset specific identity markers and independently of the region
243 of origin (Fig. 4C). Furthermore, the top 15 DEGs of each cluster were comparable between
244 both investigated regions (Sup. Fig 4A). The *bona fide* ILC identity of the selected clusters
245 was confirmed by the lack of (co)-expression of markers characteristic of other immune cell
246 types of the CNS (Sup. Fig. 4B). No CLP or ILCp cells were identified, as demonstrated by
247 the absence of a cluster of *Cd34* and *Flt3* or *Zbtb16* and *Tcf7* co-expressing cells, respectively
248 (Sup. Fig. 4C). ScRNA-seq and flow cytometry analysis showed a similar region-specific
249 subset distribution as the one observed in young adults, with group 1 ILCs as the main subset
250 in the brain, closely followed by ILC2s and ILC3s. In the dura, ILC2s clearly appeared as the
251 main ILC population (Fig. 4E).

252 We observed clear expression of signature ILC markers such as *Id2*, *Thy1*, *Rora*, *Arg1*, and
253 *Cxcr6* among postnatal CNS ILCs (Fig. 4F). Brain and dura NK cells showed expression of
254 *Eomes* and the integrin *Itga2* while ILC1s expressed higher levels of *Cd200r1* and *Itga1* (Fig.
255 4F). Furthermore, both populations of group 1 ILCs showed low *Tnf* but significant levels of
256 *Ifng*, and *Ccl3* expression (Fig. 4F). Brain and dura ILC2s expressed similar levels of *Gata3*,

257 *Icos*, and the IL25 and IL33 receptor subunits *Il1r1* and *Il2ra* (Fig. 4F). Additionally, no or very
258 low expression of *Il18r1* was detected together with expression of effector cytokines such as
259 *Il4* and *Il13* (Fig. 4F), indicating predominant presence of more differentiated ILC2s. On the
260 other hand, ILC3s were the population with higher expression of *Il7r* and *Thy1*, and molecules
261 involved in ILC3 stability such as *Batf* and *Tox2* (Fig. 4F). Transcripts for both LTi (*Ccr6*, *Cxcr5*,
262 *Lta* and *Tnfsf11*) and NKp46⁺ ILC3s (*Il2rb*, *Tbx21*, *Cd226*, *Cxcr3*, *Ccl5* and *Ncr1*) were
263 observed (Fig. 4F). Of note, *Tnf*, but not *Il22* or *Il17f*, appeared as the main cytokine produced
264 by CNS ILC3s at this developmental timepoint (Fig. 4F). Comparison of the expression of
265 helper ILC-related chemokine, cytokines, and a plethora of cell receptors showed significant
266 subset-specific but also compartment-specific ILC features. As demonstrated for adult ILCs
267 (Sup. Fig. 1I) all CNS ILCs expressed high levels of the key mediators of migration *Ccr2* and
268 *Cxcr6* (Fig. 4G). Of interest, ILC1s, especially within the brain, express *Ccr5*, *Cxcr3* as well as
269 *Ccl3*, *Ccl4* and *Ccl5* (Fig. 4G), and high levels of *Ifng* and *Tnf* (Sup. Fig. 4D). In contrast, ILC2s
270 showed higher expression of different effector cytokines and chemokines such as *Ccl1*,
271 *Cxcl10*, *Csf2*, *Il5*, and *Il13*, when located within the dura (Fig. 4G; Sup. Fig. 4D). The analysis
272 of receptors involved in a possible response of CNS ILCs to neuropeptides, hormones, or
273 metabolic signals (Sup. Table 2) indicated that, purinergic receptor (*P2rx4*), androgen receptor
274 (*Ar*), prostaglandin receptors (*Ptger4*, *Ptgir*) or lipid receptor (*Cysl1r1*) transcripts were
275 enriched in ILC2s, again especially within the dura (Fig. 4G). This points to a higher ability of
276 ILC2s to respond to neuroendocrine stimuli.

277

278 **Postnatal group 3 ILCs (incl. LTi and NKp46⁺ ILC3s) retraction results from ILC3 to** 279 **ILC1 conversion and decreased cell turnover**

280 To understand the mechanisms underlying ILC3 retraction from the developing brain, we
281 performed hallmark pathway enrichment analysis based on the ILC3 cluster-specific genes
282 (Fig. 5A). Interestingly, we observed highest activation of genes related to cell survival
283 pathways such as the apoptosis and IL2/Stat5 signaling pathways (Fig. 5A). Further analysis
284 showed that the ILC3 cluster appeared enriched in anti-apoptotic genes such as *Bcl2*, *Bcl2l1*,
285 *Mcl1* and *Cflar*, in conjunction with key autophagy related genes (*Atg3*, *Atg7*, *Lamp1* or
286 *Lamp2*) (Fig. 5B). This translated into a significantly higher ratio between the anti-apoptotic
287 (*Bcl-2*) and the pro-apoptotic (*Bim*) molecules in ILC3s when compared to ILC1s (Fig. 5C),
288 and low levels of ILC3 apoptosis measured by Annexin V and PI staining (data not shown). Of
289 interest, although postnatal CNS ILCs progressively decrease their proliferative capacity (Fig.
290 3G), when assigning cell cycle scores based on the expression of S and G2M-associated
291 genes, we identified not only a cluster of actively proliferating cells (cluster 4) but also a high
292 proportion of cells in G2M phase distributed along the different ILC clusters (Fig. 5D). Cluster
293 4, enriched in proliferating cells, was found in similar proportion in brain and dura mater (Fig.

294 4E), and was enriched in group 1 ILCs and ILC2s (Fig. 5E, F). Flow cytometry analysis
295 confirmed this data and showed ILC3s as the population with the lowest proliferation rate,
296 especially brain ILC3s, which completely stop proliferating in later developmental timepoints
297 (Fig. 3G; Fig. 5F). Overall, this indicated that ILC3s appeared to decrease their proliferation
298 capacity while activating pro-survival mechanisms in the postnatal brain.

299 To further characterize the ILC3 population present in the developing CNS, we analyzed ILC3
300 subsets pre- and postnatally as well as in 5-week-old animals. As depicted in Fig. 6, CD4⁺/
301 CCR6⁺ LTi cells, NKp46⁺ ILC3s and double-negative ILC3s were all present at perinatal stages
302 (Fig. 6A; Sup. Fig. 5A). CD4⁺CCR6⁺ LTi cells and double-negative ILC3s, appeared as the
303 main populations until P9, whereas NKp46⁺ ILC3s first appeared at P1 and peaked at P15
304 (Fig. 6A; Sup. Fig. 5A). Corroborating these results, unsupervised clustering conducted on the
305 ILC1 and ILC3 superclusters of our scRNA-seq data from P9.5 mice, revealed 4 subclusters
306 with top 15 DEGs: ILC1 (cluster 0: i.e. *Tbx21*, *Xcl1*, *Nkg7* and *Ifng*), NKp46⁺ ILC3 (cluster 1;
307 i.e. *Il7r*, *Rorc* and intermediate expression of *Il2rb*, *Ncr1*, and *Klrk1*), LTi (cluster 2; i.e. *Ccr6*,
308 *Cd4*, *Cxcr5*, *Tnfrsf11* and *Il17f*) and a small cluster with low quality cells of unclear origin named
309 as others (cluster 3; i.e. *Rgs4*, *Rgs7*, *Dmt1*, *Celf4*, and *Rtn1*) (Fig. 6B; Sup. Fig. 5B, C). Similar
310 prevalence of the identified clusters was observed in brain and dura (Sup. Fig. 5D), although
311 we clearly observed that ILC3s were predominantly located in the brain (and leptomeninges)
312 (Fig. 4A; Fig. 4E). As previously shown, besides the changes in the prevalence of the different
313 RORγt⁺ ILC subsets along development, a general contraction of this compartment was
314 underlying the CNS maturation into adulthood (Fig. 3D, E; Fig. 4A; Sup. Fig. 5A). We
315 demonstrated a pronounced decrease in ILC3 turnover as the CNS developed (Fig. 3G, Fig.
316 4G-I), which was consistent among all ILC3 subtypes (Sup. Fig. 5E). No increased cell death
317 was observed, however gene ontology pathway enrichment analysis based on the NKp46⁺/
318 ILC3 and LTi subclusters-specific genes showed 1) high activation of pathways associated to
319 active chemokine/cytokine signaling and leukocyte adhesion and, 2) upregulation of gene sets
320 related to mononuclear/myeloid-leukocyte differentiation (Fig. 6C). To analyze possible
321 plasticity events underlying this immune activation and differentiation, we performed
322 pseudotime and trajectory analysis using Monocle 3 (cluster 1 as origin). A potential trajectory
323 path was observed originating from NKp46⁺ ILC3 cluster and branching on one side towards
324 the LTi cluster (2) and on the other side towards the ILC1 cluster (0) (Fig. 6D). Gradual
325 decreased expression of ILC3-associated markers (*Tcf7*, *Tcrg-1*, *Tcrg-2*, *Ddc*), while
326 increasing ILC1 markers such as *Cd52*, *Il2rb*, *Klrk1*, *Xcl1* or *Gimap4*, was observed along the
327 NKp46⁺ ILC3 > ILC1 trajectory (clusters 1>0) (Fig. 6E). To confirm this assumption, brains of
328 RORγt-FM mice were analyzed at different ages. A population of ex-ILC3s emerged at P9,
329 13.9 ± 1.2% (brain) and 8.04 ± 1.7% (dura mater), which was accompanied by a peak in the
330 presence of double-positive RORγt⁺Tbet⁺ ILCs (Fig. 6F). Furthermore, although the double

331 positive ROR γ ⁺Tbet⁺ intermediate population and ILC3s almost completely disappeared at
332 later timepoints, the frequency of ex-ILC3s among Tbet⁺ ILC1s remained stable (between 10-
333 20%) throughout life (Fig. 6F; Fig. 4A). Overall, this indicated that ROR γ ⁺ ILCs retraction from
334 the developing brain is also partially mediated by an *in situ* ILC3 to ILC1 conversion, probably,
335 in response to changes in the tissue microenvironment.

336

337 **Postnatal brain ILCs show an increased type 1 immune response**

338 Next, to decipher possible local environmental features underlying the ILC3 to ILC1 conversion
339 occurring predominantly within the brain, we compared the brain-specific ILC gene signatures
340 with the dura as a reference compartment. Considering total ILCs, only 23 genes, appeared
341 differentially expressed predominantly in brain by fold-change above or below 0.5/-0.5. The
342 identified pattern was enriched in AP-1 components (*Junb*, *Fos*, *Fosb*, *Zfp36*) and GTPases
343 of the immunity-associated proteins (GIMAPs: *Gimap3*, *Gimap4*, *Gimap5*, *Gimap6*), indicating
344 higher immune activation and active modulation of cell survival/death pathways in brain ILCs
345 (Fig. 7A). Gene set enrichment analysis (GSEA) of normalized counts showed an activated
346 status of brain cells, characterized by the upregulation of gene ontology (GO) biological
347 process (BP) pathways such as “response to calcium” and “activation of immune response”.
348 In contrast, dura ILCs were enriched in metabolic-related pathways such as “small molecule
349 metabolic process”, “ATP metabolic process” or “aerobic respiration” (Fig. 7B). The analysis
350 of each brain ILC-subset separately revealed that for ILC1, ILC2, and ILC3, 189, 554, and 107
351 genes, were differentially expressed respectively, by fold-change above or below 0.8/-0.8 and
352 Fisher p value < 0.05 (Fig. 7C). Gene set analysis (GSA) of the hallmark gene sets using the
353 subset-specific identified DEGs and GSEA of normalized counts further confirmed that ILCs
354 in the brain tended to express genes related to active immune response and differentiation
355 (GSA-Hallmark: “allograft rejection”, “Tnfa signaling via NFKB”, “Interferon gamma and alpha
356 response” and “reactive oxygen species pathway”); whereas ILCs in the dura showed higher
357 activation of proliferative and metabolic-associated pathways (GSA-Hallmark: “Myc targets V1
358 and V2”, “oxidative phosphorylation” and “fatty acid metabolism”) (Fig. 7D). Interestingly, this
359 active immune status within the brain was associated with type I signaling pathways (i.e. TNFa
360 or interferon alpha/gamma immune response) (Fig. 7D).

361

362 **Perinatal group 3 ILCs are functionally active and contribute to dura lymphatic** 363 **development.**

364 To investigate the functional meaning of the transitory presence of ILC3, we assessed the
365 production of IL-22, IL17a, TNF α and IFN γ of ROR γ ⁺ ILCs in perinatal stages E18 and P1,
366 upon stimulation with Ionomycin/PMA. In contrast to P9 (Sup. Fig. 4D), we observed significant
367 production of IL-22, but especially IL17a, among group 3 ILCs at earlier developmental

368 timepoints (E18 and P1) (Fig. 7A). Interestingly, a peak in the production of the $TNF\alpha$ at P1,
369 even before appearance of $NKp46^+$ ILC3s, was detected (Fig. 7A). Among other signaling
370 molecules, production of $TNF\alpha$ by ILC3s has been reported to be necessary for the formation
371 of the gut associated lymphoid tissue³⁵. Thus, we questioned whether the CNS $ROR\gamma^+$ ILCs
372 could be involved in the formation of the lymphatic structures of the brain, i.e. the lymphatic
373 vessels located within the sinuses of the dura meningeal layer, which have been reported to
374 have the ability to acquire lymphoid-tissue like properties in the context of neuroimmune
375 inflammation³⁶⁻³⁸. As shown in Fig. 7B, whole-mount dura meningeal expressed the
376 endothelial lymphatic cell marker Lyve-1, podoplanin and showed intermediate expression of
377 CD31 (Fig. 7B, zoomed images). In contrast, $ROR\gamma^{GFP/GFP}$ mice lacking $ROR\gamma^+$ ILCs and
378 Th17 cells, but not T cell-deficient $Rag1^{-/-}$ mice, showed a diminished expression of Lyve-1⁺
379 positive structures along the dural sinuses (Fig. 7C, D). This effect was observed both in adult
380 mice (3m) and in 3-week-old mice (3wo), timepoint in which dura lymphatic vessels are
381 reported to reach complete development³⁹ (Fig. 7C, D). Expression analysis of lymphatic
382 endothelial markers in the meninges of these mice also revealed a significant decrease of
383 Lyve-1 and Flt4 expression, and a mild reduction of Prox1 and podoplanin, exclusively in
384 $ROR\gamma^{GFP/GFP}$ animals (Fig. 7E). Altogether, our data indicates that $ROR\gamma^+$ ILCs, transiently
385 present in the developing brain, play a role in the establishment of the lymphatic vessels of
386 the dura meningeal layer.

387

388 Discussion

389 The important role of the immune system in brain development and homeostasis has been
390 revealed during the last decade⁴⁰⁻⁴². Investigations on the implication of ILCs in such
391 processes are however limited by their low prevalence within the healthy brain and the lack of
392 knowledge regarding CNS ILC niche formation, maintenance, and functions. Using
393 intravenous labeling and lineage-specific markers we describe here the full spectrum of *bona*
394 *fide* resident ILCs in the healthy young adult CNS, which showed a compartment-specific
395 distribution of differentiated cells. In line with previous studies^{6,25,33}, we showed that group 1
396 ILCs, including ILC1 ($NK1.1^+NKp46^+CD122^+CD90.2^+CD200R^{int}Tbet^+Eomes^-$) and NK cells
397 ($NK1.1^+NKp46^+CD122^+CD90.2^{+/-}CD200R^-Tbet^+Eomes^+$), appeared predominantly located in
398 inner brain structures (choroid plexus and brain parenchyma with leptomeninges), while ILC2s
399 ($CD127^+CD90.2^+CD25^+ST2^+CD200R^{high}Gata3^+$) were highly enriched in the dura meningeal
400 layer. CNS ILCs of both, male and female young adult mice constituted a small population of
401 mature lymphocytes that displayed a quiescent state with low basal levels of proliferative
402 capacities and functional activation. This may suggest that in the normal developed brain
403 compartments, innate lymphoid cells present low levels of basal activity and are able to

404 promptly react to different stimuli, as reported by us and others in the context of autoimmune
405 inflammation⁶, spinal cord injury³⁰ or aging²⁶. Interestingly, the presence of an ex-ILC3
406 population, principally among Tbet⁺RORγt⁻ ILC1s, pointed to dynamic changes in the CNS-
407 ILC compartment during early life. To understand these changes, we have examined for the
408 first time when and how the ILC compartment of the CNS is established and unraveled an
409 important functional implication of perinatal ILC3s in CNS development and homeostasis.
410 The murine CNS is predominantly devoid of adaptive immune cells (T and B cells) at birth^{40,41}.
411 However, ILCs have been reported to start seeding peripheral tissues during fetal
412 development in the form of progenitor cells and mature ILCs, appearing as early as E14.5 in
413 tissues such as the intestine^{10,11} or the liver¹⁵. We therefore investigated ILC presence in the
414 CNS (focusing on whole brain without dura meninges) pre- and postnatally using the Id2^{GFP}-
415 reporter line. Our data revealed a first appearance of Id2⁺CD45⁺LinLD⁻CD3⁻CD5⁻CD127^{+/-}
416 CD122^{+/-} cells in the embryonal CNS, between E14 and E16. Although no CLPs were found
417 within the CNS, we identified a small proportion of ILCs expressing high levels of α4β7, PD-1
418 and PLZF, and co-expressing intermediate levels of Gata3, T-bet and RORγt. This is
419 compatible with a ILC progenitor-like identity, able to further differentiate into different ILC
420 subsets¹⁰. The presence of this progenitor-like ILC population within the CNS supports the
421 concept of brain seeding and *in situ* differentiation of ILC progenitor cells in non-hematopoietic
422 organs during embryogenesis, as previously reported for intestine or lung^{10,11}. Nevertheless,
423 progenitor-like ILC cells seem to disappear from the CNS later in life as no cells with a
424 progenitor identity were detected in our sequencing analysis at P9.5. We found, on the other
425 hand, differentiated ILCs already at E16, indicating that the CNS ILC niche arises from both,
426 *in situ* differentiation and expansion, as well as different waves of peripheral infiltration,
427 mimicking mechanisms of layered ontogeny previously reported in peripheral organs^{9,11,15,43}.
428 In this line, we detected that brain embryonal Eomes⁻ and Eomes⁺ group 1 ILCs decreased
429 their proliferation postnatally coinciding with a second wave of brain infiltrating Eomes⁺ cells.
430 This second wave of infiltration occurred in parallel to the increase of Eomes⁺ group 1 ILCs in
431 the peripheral circulation. In contrast, CNS ILC2s appeared to originate postnatally, as the
432 main influx of ILC2s into the CNS occurs after the first week of life, concurrently with an
433 increase in circulatory ILC2s. The dynamics of postnatal ILC2 infiltration coincides with those
434 reported for other peripheral organs^{9,44}. Finally, we showed a transitory presence of
435 embryonal-derived ILC3s that disappear from the CNS after the first weeks of life. This ILC3
436 cell cluster seemed to mainly originate from embryonal ILCs that differentiate and/or expand
437 within the perinatal brain as no significant numbers of circulating RORγt⁺ ILCs were observed
438 at postnatal timepoints.
439 Altogether, we defined for the first time that the formation of the CNS ILC pool is established
440 during the embryonal and postnatal life, since no further signs of infiltrating ILCs (besides a

441 small fraction of NK cells) was observed in the healthy adult brain. Furthermore, we showed
442 that group 1 ILCs and in lower levels, brain ILC2s and ILC3s, expressed type-1 associated
443 chemokine receptors transcripts *Ccr5* and *Cxcr3*, whose ligands, CCL5 and CXCL9/10, have
444 been reported to be expressed by brain-derived cells such as astrocytes⁴⁵ or microglia⁴⁶,
445 respectively. This further suggests an implication of these chemokines in the perinatal iLC
446 infiltration of the brain.

447 The postnatal ILC composition observed by flow cytometry was confirmed by scRNA-
448 sequencing. We identified the complete spectrum of mature ILCs in newborn brain and dura
449 matter, including group 1 ILCs (NK and ILC1s), ILC2s and ILC3s, with phenotypical and
450 functional characteristics that resemble the ones obtained for peripheral tissues^{10,47}. The
451 compartment-specific separation observed in adult brains was already apparent in the
452 newborn, with active group 1 ILCs enriched and proliferating in brain, while ILC2s were found
453 more prevalent in the dura. This interesting compartmentalization also resembles that of other
454 tissues, such as the lung or the liver, in which ILC2s are prominently localized at epithelial and
455 fibroblast-rich barriers whereas type 1 lymphocytes accumulate within the parenchymal
456 space^{15,48}. In the lung, it has been reported that ILC1s control proliferation, infiltration and
457 activation of ILC2s in an IFN γ -mediated manner^{48,49}. Interestingly, our pathway analysis of the
458 differentially expressed genes for each ILC subset in P9.5 showed an upregulation of genes
459 related to IFN γ response especially in brain ILCs. Moreover, while ILC1 appears to be
460 activated in this brain milieu, ILC2s and ILC3s displayed an increased expression of stress-
461 response pathways, including reactive oxygen species production and hypoxia. Thus, the
462 postnatal “inflammatory” parenchymal environment may favor survival and functionality of
463 ILC1s, restraining other ILC subtypes, predominantly ILC2s, to meningeal barriers.
464 Intriguingly, processes such as neurogenesis, synapse formation/pruning and blood-brain
465 barrier formation, that may contribute to a state of controlled, focal tissue inflammation and
466 lower nutrient and oxygen availability, are highly activated during the postnatal window in
467 rodents^{50,51}.

468 Focusing on the ROR γ t⁺ ILCs, the ILC3 pool shifted from being enriched prenatally with LTi
469 cells to be composed principally by double negative and NKp46⁺ ILC3s after birth. Several
470 processes appeared to be underlying the contraction of the ROR γ t⁺ population after the first
471 week of life. First, in contrast to the basal levels of proliferation observed in group 1 and 2
472 ILCs, the ILC3 compartment seems to almost stop proliferating after birth, while upregulating
473 expression of anti-apoptotic machinery mediators such as Bcl-2. Of note, Bcl-2 expression
474 has been reported to fluctuate following changes in local cytokine signals such as IL-7⁵².
475 Furthermore, we observed an increased expression of many autophagy-related genes (*Atg3*,
476 *Atg7*, *Atg12*, *Lamp1* or *Lamp2*), suggesting ongoing processes of intracellular organelle

477 degradation, which has been implicated in ILC survival⁵³. This, together with the postnatal
478 absence of peripheral blood circulating ROR γ ⁺ ILCs, translates into a drastic decrease of
479 ROR γ ⁺ cell turnover within the postnatal brain. This resembles the ILC3 transitory presence
480 also reported in the neonatal thymus, in which ILC3 also declined in numbers after birth while
481 ILC2 becomes the main thymic ILC population⁵⁴. In addition, analysis of ROR γ ⁺-FM mice
482 revealed the occurrence of *in situ* ILC3 to ILC1 conversion at postnatal day 9, a timepoint in
483 which cells with a mixed phenotype were detected by both flow cytometry and single-cell
484 sequencing analysis. The observed postnatal plasticity suggests that adult CNS ex-ILC3s are
485 long-lived cells that originated during these first weeks of life as a reminiscence of the perinatal
486 presence of ROR γ ⁺ ILCs. Indeed, presence of embryonal derived ILCs have been reported
487 also in other adult tissues^{9,12,15}, proving the ability of these cells to remain as long-life cell
488 within the tissue. Finally, the activation of inflammation-related and cytokine signaling
489 pathways (type 1 immune response) that seems to occur within the postnatal brain could also
490 contribute to the contraction of ILC3s from the brain and the concurrent ILC3 to ILC1
491 conversion as reported in peripheral tissues in both, human⁵⁵ and mice^{20,56,57}.

492 On the functional level, we observed high levels of TNF α production by ILC3s at pre- and
493 postnatal timepoints. ROR γ ⁺ lymphocytes associated signaling molecules such as TNF and
494 LT α seem to be necessary for the development of secondary lymphoid structures, including
495 lymph nodes but also the intestinal associated lymphoid tissue, Peyer's patches (PPs)^{35,58,59}.
496 In line with this, we showed here that the absence of ROR γ ⁺ ILCs in the developing brain
497 affected the formation of the newly described lymphatic vessels of the dura mater⁶⁰. This was
498 already observed at P15, timepoint in which the dura lymphatic vessel formation should be
499 completed³⁹. It has been shown that vascular endothelial growth factor C (VEGF-C)/VEGF
500 receptor 3 (VEGFR3) signaling is essential for the formation of these lymphatic vessels⁶¹.
501 However, TNF α appears to also cooperate with this axis in the promotion of
502 lymphangiogenesis, through indirect activation of tissue macrophages during pathological
503 conditions such as cancer⁶². Due to the unique timeline of dura lymphatic formation, we could
504 speculate that TNF α - production by perinatal ILC3s contribute to the process of dura lymphatic
505 formation, revealing an unique involvement of ROR γ ⁺ ILCs-derived signaling in dural
506 lymphangiogenesis.

507

508

509

510

511

512

513 **Methods**

514

515 **Mice**

516 *Rorc*^{m2^{litt}/J} mice (Eberl et al., (2004))⁶³, used as *Rorc*(gt)^{GFP/GFP} and *Rorc*(gt)^{GFP/+} mice, *Id2*^{GFP/+}
517 mice (Rawlins et al., (2009))⁶⁴ and *Rag1*^{-/-} mice (Mombaerts et al., (1992))⁶⁵ were provided by
518 Andreas Diefenbach (Charité-Universitätsmedizin Berlin, Berlin) and bred in our animal
519 facility. *Rorc*(gt)-Cre^{Tg} (Eberl et al., (2004))⁶³ mice crossed to *Rosa26RE*^{eYFP} mice (Srinivas
520 et al., (2001))⁶⁶, used as *Rorc*(gt)-fate mapping animals, were provided by Chiara Romagnani
521 (DRFZ, Berlin) and bred in our animal facility. *Rorc*(gt)-cre was carried only by female breeders
522 to prevent germline YFP expression. Non-transgenic experiments were performed with female
523 and male, wild-type C57BL/6J mice purchased from the Research Institute for Experimental
524 Medicine (FEM) of the Charité (Berlin, Germany) and Charles River Laboratories (Freiburg,
525 Germany). All mice used were between 8 to 16 weeks old, unless indicated otherwise. Animal
526 were pooled, when necessary, as indicated along the text.

527 All mice were bred under specific pathogen-free conditions in the Research Institute for
528 Experimental Medicine of the Charité (Berlin, Germany). Animal handling and experiments
529 were conducted according to the German and European animal protection laws and approved
530 by the responsible governmental and local authority (Landesamt für Gesundheit und
531 Soziales).

532

533 **Organ collection**

534 Peripheral blood samples were collected in tubes with 2 mM EDTA at room temperature from
535 euthanized mice before perfusion with 1-5 mL (embryos), 5-10 mL (pups) and 40-50 mL
536 (adults) of ice-cold PBS. The rest of the organs: brain and spinal cord (with pia matter), choroid
537 plexus, dura meninges (including partially arachnoid meninges), spleen, lymph nodes and liver
538 were collected on ice-cold medium/PBS and processed immediately. For RT-qPCR, samples
539 were lysed in RLT buffer (lysis buffer) and stored at -20°C. For immunofluorescence,
540 transcardial perfusion with ice-cold PBS was followed by perfusion with 10-20 mL of buffered
541 4% paraformaldehyde (PFA, EMS).

542

543 **Tissue processing**

544 The CNS (brain and/or spinal cord) was mechanically homogenized and passed through a 70
545 µm cell strainer (Corning) with complete medium [RPMI-1640 supplemented with 2 mM L-
546 glutamine (Gibco), 100 U/mL penicillin (Seromed), 100 µg/mL streptomycin (Seromed), 10%
547 FCS (Sigma–Aldrich) and 1% HEPES (Gibco)]. After centrifugation at 400 g for 15 min at 4°C,
548 the pellet was resuspended in 5mL of 40% Percoll (GE Healthcare) and the lymphocytes were

549 collected from the pellet after centrifugation at 2,200 g. Erythrocyte lysis was performed when
550 necessary for 5 min at room temperature in between the two following washing steps done
551 with PBS/BSA.

552 For the analysis of the choroid plexus separately from the brain parenchyma, the tissue was
553 removed under a dissecting microscope from the lateral, third and fourth brain ventricles, and
554 processed in parallel. Brain parenchyma processing was performed as described above.
555 Isolated choroid plexuses were digested in 500 μ L PBS containing 1 mg/ml
556 Collagenase/Dispase (Sigma) and 1 mg/mL DNase I (Sigma) for 20 min at 37°C with 400 rpm.
557 In parallel, the dura meninges were peeled off from the interior side of the skull cap and
558 digested in 500 μ L PBS containing 2.5 mg/ml collagenase type VIII from Clostridium
559 Histolyticum (Sigma) and 1 mg/ml DNase I (Sigma) for 20 min at 37°C with 400 rpm. After
560 digestion, both tissues were passed through a 70 μ m cell strainer (Corning) and centrifuge at
561 400 g for 10 min.

562 Single cell suspensions of spleen, lymph nodes and liver were obtained by homogenizing the
563 tissue through a 100 μ m cell strainer (Corning). The spleen and blood underwent erythrocyte
564 lysis for 10 min and washed one or two times as needed. Liver lymphocytes were enriched
565 after mechanical dissociation and homogenization through a 100 μ m cell strainer by
566 centrifuging at 50 g for 1 min and discard the pellet.

567

568 **Labelling of the vascular compartment**

569 To distinguish vasculature-associated circulating cells from those residing within the CNS, 2
570 μ g/200 μ l of PE anti-mouse CD45.2 antibody (Biolegend, 30-F11) diluted in PBS solution were
571 injected through the tail vein. Animals were sacrificed 3 min post-injection.

572

573 **Flow cytometry**

574 Extracellular flow cytometry staining was performed at 4°C in PBS containing 0.5% BSA. Dead
575 cells were excluded by staining with Fixable Viability Dye (LD) (eBioscience, 1:4,000). Then,
576 Fc receptors were blocked by incubating 15 min with anti-mouse CD16/CD32 (clone 2.4G2,
577 BD Biosciences). The following antibodies were used for staining: PerCP anti-mouse CD45
578 (Biolegend, 30-F11, 1:100) or BUV496 anti-mouse CD45 (BD, 30-F11, 1:100), APC-Cy7 anti
579 mouse/human CD45R/B220 (Biolegend, RA3-6B2, 1:100), APC-eFluor 780 anti-mouse
580 CD45R/B220 (eBioscience, RA3-6B2, 1:100), APC-eFluor 780 anti-mouse CD19
581 (eBioscience, eBio1D3, 1:100-1:200), APC-Cy7 anti mouse-CD11b (BD, M1/70, 1:50), APC-
582 eFluor 780 anti-mouse CD11b (eBioscience, M1/70, 1:50), APC-eFluor 780 anti-mouse Gr-1
583 (eBioscience, RB6-8C5, 1:100), APC-eFluor 780 anti-mouse Fc ϵ RI (eBioscience, MAR-1,
584 1:200), APC-Cy7 anti mouse F4/80 (Biolegend, BM8, 1:100), APC-eFluor 780 anti-mouse
585 F4/80 (eBioscience, BM8, 1:100), APC-eFluor 780 anti-mouse CD11c (eBioscience, N418,

586 1:100), BV650 (Biolegend, 17A2, 1:50) or PerCP-Vio 700 (Miltenyi, REA641, 1:200) anti-
587 mouse CD3, BV510 anti-mouse CD4 (Biolegend, RM4-5, 1:50), PE anti-mouse CD5
588 (Biolegend, 53-7.3, 1:300), PE-Cy7 (Biolegend, 1:50), PE (Biolegend, 1:100) or BV421
589 (Biolegend, 1:50) anti-mouse CD127 (A7R34), biotin (Biolegend, 1:200) or PE-Cy5
590 (Biolegend, 1:300) anti-mouse CD122 (TM- β 1), Streptavidin-PE-Cy5 (1:300), PE anti-mouse
591 CD200R (Biolegend, OX110, 1:200), Alexa Fluor 700 anti-mouse CD90.2 (Biolegend, 30-
592 H12, 1:100), APC (Biolegend, 1:50), BV711 (Invitrogen, 1:50) or BUV395 (BD Horizon,
593 29A1.4, 1:50) anti-mouse NKp46 (29A1.4), BV421 anti-mouse α 4 β 7 (BD, DATK32, 1:100),
594 BV421 (Biolegend, 1:50) and PerCP Cy5.5 (Biolegend, 1:50) anti-mouse ST2 (DIH9), BV605
595 (Biolegend, 1:50) and BV510 (Biolegend, 1:50) anti-mouse CD25 (PC61), PE-Vio615 anti-
596 mouse CXCR5 (Miltenyi, REA215, 1:50), PE anti-mouse CD135 (Biolegend, A2F10, 1:100),
597 BV605 anti-mouse c-Kit (Biolegend, ACK2, 1:100), BV510 anti-mouse CXCR3 (Biolegend,
598 CXCR3-173, 1:50), PE anti-mouse CXCR6 (eBioscience, DANID2, 1:50), BV510 anti-mouse
599 PD-1 (BioLegend, 29F.1A12, 1:100), BV605 anti-mouse CD196 (CCR6) (Biolegend, 29-2L17,
600 1:200) and PE and PE-Vio770 anti-mouse NK1.1 (Miltenyi, REA1162, 1:50).

601 For intracellular and intranuclear staining, the FoxP3 transcription factor staining buffer set
602 (Invitrogen) was used to fix and permeabilize the cells according to the manufacturer's
603 instructions. In case of reporter or fate-map GFP/YFP signal, cells were fixed for 20 min at
604 room temperature with 2% PFA (EMS) before beginning with the FoxP3 staining protocol.
605 Cells were stained with BV711 (1:50) or AlexaFluor647 (1:300) anti-mouse T-bet (Biolegend,
606 4B10), PE eFluor610 anti-mouse Eomes (Biolegend, Dan11mag, 1:200), AlexaFluor488
607 (1:50) or AlexaFluor647 (1:50) anti-mouse Gata3 (Biolegend, 16E10A23), PE (BD, 1:500) or
608 BV786 (BD, 1:100), anti-mouse ROR γ t (Q31-378), AlexaFluor647 anti-mouse/human PLZF
609 (BD, R17-809, 1:800), PerCP-eFluor 710 anti-mouse Ki67 (eBioscience, SolA15, 1:1000),
610 AlexaFluor488 anti-mouse Bim (Cell Signaling, C34C5, 1:100), AlexaFluor488 rabbit anti-
611 mouse mAb IgG XP Isotype Control (Cell Signaling, DA1E, 1:100), PE-Vio770 anti-mouse
612 Bcl-2 (Miltenyi, REA356, 1:100) and PE-Vio770 human anti-mouse IgG1 (Miltenyi, REA294,
613 1:100). Apoptosis analysis was done with the APC Annexin V (1:50) apoptosis detection kit
614 with PI (1:200) in Annexin V Binding Buffer (Biolegend).

615 For the analysis of cytokine production, CNS derived single-cell suspension were stimulated
616 in 96 well plates in complete medium with PMA (10ng/ml, Sigma-Aldrich) and Ionomycin
617 (500ng/ml, Sigma-Aldrich), and cell transport inhibitor Brefeldin A (10 μ g/ml, Biolegend) was
618 added 1 hour later for a total incubation time of 4 hours at 37°C. After washing, cells were
619 extracellularly stained and fixed with 2% PFA (EMS) for 20 min at room temperature. Once
620 cells were fixed, the FoxP3 staining kit was used again to do a second fixation and
621 permeabilization. Cells were then stained with PE anti-mouse IFN γ (Biolegend, XMG1.2,
622 1:100), APC anti-mouse TNF α (BD Bioscience, MP6-XT22, 1:50), PE anti-mouse IL-17A

623 (Biolegend, TC11-18H10.1, 1:200) and PerCP Cy5.5 anti-mouse IL-22 (Biolegend, Poly5164,
624 1:25) for 45 min at room temperature.

625 Sample acquisition was performed using a LSR Fortessa flow cytometer (BD Biosciences).
626 Data were further analyzed in FlowJo Software v.10 (FlowJo). Gating of populations were
627 defined with fluorescence minus one (FMO) staining controls when necessary. Flow cytometry
628 plots are shown as contour plots (5% with outliers). Overlay histograms were normalized to
629 mode.

630

631 **Immunofluorescence staining and image analysis**

632 Transcardially perfused mice were decapitated immediately and the skull cap was removed
633 and clean of overlying skin and muscle before being drop fixed in 2% PFA at 4°C for 24 hours
634 and washed with PBS for another 24 hours. The dura/arachnoid was then carefully peeled
635 from the skull cap using fine surgical forceps and stored in PBS at 4°C. Whole mounts were
636 stained in 24-well plates with constant agitation following the same protocol as in Louveau et
637 al., (2015)⁶⁰. WT animals and mutant were always stained in parallel for paired comparison.
638 First, they were blocked and permeabilized with PBS containing 2% horse serum, 1% BSA,
639 0.1% Triton-X-100 and 0.05% of Tween 20 for 1 hour at room temperature, followed by
640 incubation with primary antibodies: purified rat anti-mouse CD31 (BD Pharmingen™, MEC
641 13.3, 1:100) overnight at 4°C in PBS containing 1% BSA and 0.5% Triton-X-100. Whole-
642 mounts were then washed 3 times for 5 min at room temperature in PBS followed by incubation
643 with Alexa Fluor 568 anti-rat (Invitrogen, 1:500) for 1 hour at room temperature in PBS with
644 1% BSA and 0.5% Triton-X-100. Meninges were washed 3 times again for 5 min at room
645 temperature in PBS and incubated with eFluor 660 anti-mouse Lyve-1 (eBioscience, ALY7,
646 1:200) and AlexaFluor488 anti-mouse Podoplanin (eBioscience, eBio8.1.1 (8.1.1), 1:200).
647 Finally, nuclei were stained with 1:10,000 DAPI reagent, mounts were washed with PBS and
648 mounted with Eprepia™ Shandon™ Immu-Mount™ under coverslips.

649 Images were acquired with a Nikon Scanning Confocal A1Rsi+ and/or a Keyence BZ-X810
650 fluorescence microscope. Image analysis was performed using FIJI plugin for ImageJ
651 (National Institutes of Health). Analysis of meningeal Lyve1 was performed measuring the
652 mean fluorescence intensity of Lyve1 of the whole dura meninges along 10 mm of Z-stack
653 images taken every 1 mm. The mean of the values obtained per plane was calculated and the
654 ratio between the mean fluorescence intensity of mutant versus its age-and gender matched
655 WT control was calculated.

656

657 **Real-time quantitative PCR (RT-qPCR)**

658 mRNA was isolated from dura meninges by using RNeasy Mini Kit (Qiagen) following the
659 manufacturer's protocol. RNA samples were further transcribed into first strand

660 complementary DNA by using High-Capacity cDNA Reverse Transcription kit (Applied
661 Biosystems). RT-qPCR reactions were assayed in triplicates per sample using a
662 QuantStudio™ 5 Real-Time PCR system and TaqMan Gene expression assays (all
663 ThermoFisher): Lyve-1 (Mm00475056_m1), Podoplanin (Mm01348912_g1), Flt4
664 (Mm01292604_m1), Prox1 (Mm00435969_m1) and Hprt (Mm03024075_m1). mRNA content
665 was normalized relative to the mean expression of the arithmetic means of Hprt CT values by
666 applying the comparative CT method ($2^{-\Delta CT}$) in which ΔCT (gene of interest) = CT (gene of
667 interest) – CT (arithmetic mean of housekeeping reference value). Furthermore, the ratio was
668 calculated based on C57BL/6J control samples.

669

670 **ILCs scRNA sequencing and analysis**

671 Brain and dura meninges were collected and processed as describe in “Tissue processing”.
672 Immune cells from P9.5 C57BL/6J mice were collected in two biological replicates with a total
673 of 10-13 pups per replicate. Cells were sorted as CD45⁺Lin^{LD}CD3⁻CD5⁻CD127⁺ and/or
674 CD122⁺ into 384-well cell-capture plates containing barcoded primers and mineral oil and,
675 immediately stored at -80°C. Plates were processed and sequenced at Single Cell Discoveries
676 (Utrecht, The Netherlands), using an adapted version of the SORT-seq protocol⁶⁷ with primers
677 described in Van den Brink et al., (2017)⁶⁸. Library preparation was done following the CEL-
678 Seq2 protocol⁶⁹ to prepare a cDNA library for sequencing using TruSeq Small RNA primers
679 (Illumina). The DNA library was paired-end sequenced on an Illumina NextSeq 500, high
680 output, with a 1 × 75 bp Illumina kit. Reads were mapped on *Mus musculus* (GRCm38) using
681 STARsolo (2.7.10a). The percentage of retained wells range between 48%-79% with 44.45 to
682 55.22 million retained reads per library. Both run results were combined and cells were filtered
683 based on the expression of 500-4000 genes with mitochondrial counts below 10%, leaving
684 480 cells from brain and 362 from dura meninges for subsequent analysis. Seurat 5.0.1 was
685 used for further analysis.

686 Dimensional reduction and clustering: Using functions of the Seurat package (v5.0.2), we first
687 perform standard pre-processing (log-normalization with the *NormalizeData()* function, scale
688 factor=10000) and identify variable features based on variance stabilization transformation for
689 which the top 2000 highly variable genes were selected (*FindVariableFeatures()* function,
690 method “vst”). Next, we scaled the integrated data using the *ScaleData()* function (“nCount”
691 and “mitochondrial percentage” were used for regression). Once differences generated from
692 technical preparations were minimized, principal component analyses (50 principal
693 components) were performed on variable genes and embedded in 2-dimensional UMAP plots.
694 We used jackstraw test to calculate the statistical significance and variance of each principal
695 component. Based on these results, we performed clustering using the
696 *FindNeighbors()* and *FindClusters()* methods with the first 12 principal components and a

697 resolution of 0.7. ILC identity was confirmed by discarding co-expression of other immune
698 cells specific genes (see Sup. Fig. 4B) and by confirming expression of canonical ILC genes
699 among the top DEGs of each cluster and assessing expression of known ILC subset marker
700 genes along the clusters (Fig. 4D, F and Sup. Fig. 4A).

701 Differential expression: Compartment (brain or dura) specific markers were then identified
702 using the Wilcoxon rank sum test implemented by the *FindAllMarkers()* methods of the Seurat
703 package. This was performed before and after correcting for the transcriptome alterations
704 induced by enzymatic digestion on dura meningeal ILCs. To do this correction, we generated
705 a list of genes reported to be associated to enzymatic digestion (Sup. Table 3)^{32,68,70} and
706 removed them from the differentially expressed genes found in dura meningeal ILCs before
707 subsequent analysis. Differential gene expression analysis between compartments for the
708 whole dataset or per cluster was done after randomized subsetting and repeated several times
709 to confirm consistency in the results. Furthermore, compartment-specific differential analysis
710 was done at the single cell level and at pseudobulk level, integrating both analysis as a final
711 step for the selection of the compartment-specific differentially expressed genes. At the single
712 cell level, the *FindAllMarkers()* function from the Seurat package based on Wilcoxon test
713 (logfc.threshold= 0.2, only.pos =FALSE, min.pct = 0.1) was used, while the Limma package
714 functions *lmFit()*, *eBayes()*, *topTable()* were used to implement empirical Bayes linear models
715 for identifying DEGs on the transformed pseudobulk data. Pseudobulk data was generated by
716 converting the Seurat object into a SingleCellExperiment object, and applying the
717 *aggregateAcrossCells()* function. The Fisher's method for combining p-values was then used
718 on the DEGs with a fold-change above or below 0.8/-0.8 in both analysis and DEGs were
719 selected based on Fisher p value < 0.05.

720 Pathway enrichment: Overrepresentation enrichment analysis with the function *enricher* from
721 the *clusterProfiler* package (v4.6.2; Wu et al.,(2021))⁷¹ was used on the cluster-specific and
722 compartment-specific differentially expressed genes to determine significantly enriched
723 Hallmark (p<0.05) and Gene Ontology (GO) terms (adj.p < 0.05 and k.K (significant genes in
724 set/total genes in set) > 0.1). In addition, the *fgsea* package (v1.24.0; Korotkevich et al.,
725 (2016))⁷² for fast pre-ranked gene set enrichment analysis (GSEA) was used on the pre-
726 ranked gene lists generated, based on the fold-change values calculated by the *FindMarkers*
727 function using the Wilcoxon rank sum test.

728 Trajectory analysis: Monocle 3 (v1.3.4)^{73,74} was used to analyze plasticity related trajectories
729 between ILC3 and ILC1 clusters. The function *as.cell_data_set()* was used to convert the
730 Seurat object into a Monocle3 object. After graph learning was performed (*learn_graph()*), we
731 ordered the cells with the function *order_cells()*, setting the starting node embedded in the
732 NKp46⁺ ILC3 cluster. Trajectories were then visualized using the *plot_cells()* function. We then
733 identified genes co-regulated along the pseudotime with the graph-autocorrelation function

734 graph_test(neighbor_graph= "principal_graph") and plotted the top 8 most significant ones in
735 graphs where cells were ordered onto a pseudotime trajectory based on these ILC3 and ILC1-
736 identity markers.

737

738 **Analysis of CNS-derived CD45⁺ immune cell scRNA-seq data**

739 Data from whole brain and micro-dissected CNS barrier-sorted immune cells generated by
740 Van Hove, et al. (2019)³² was downloaded and analyzed using Seurat standard workflow (see
741 above). ILC clusters were identified by excluding clusters with expression for other CNS-
742 immune cells and selecting those with the highest ILC gene expression score (depicted in
743 Sup. Table 1).

744

745 **Statistical analysis**

746 GraphPad Prism 9 was used for statistical analysis. Whitney test for two group comparisons
747 and Kruskal-Wallis test with Dunn's for multiple comparison were used for statistical analysis.
748 P values of $p > 0.05$ were considered as not significant, P values were considered as followed:
749 * $p < 0.05$, ** $p < 0.01$, *** $p < 0.001$. Figures show bars or dots indicating mean \pm SEM unless
750 stated. Due to the exploratory nature of the study, a power calculation was not performed to
751 determine the sample size of each group. Therefore, a rule of minimum three animals to
752 maximum eight animals per group was set for data sampling. Data analysis was not performed
753 blindly to the experimental conditions.

754

755 **Data analysis and visualization**

756 Data was analysed using several specialized tools depending on the technique (Flowjo,
757 Graphpad Prism, R v5.0.2, ImageJ) and figures were created and edited in Adobe Illustrator.

758

759

760

761

762

763

764

765

766

767

768

769

770

771

772

773

774

775

776

777 References and notes

- 778 1. Vivier, E., Artis, D., Colonna, M., Diefenbach, A., Di Santo, J.P., Eberl, G., Koyasu, S., Locksley,
779 R.M., McKenzie, A.N.J., Mebius, R.E., et al. (2018). Innate Lymphoid Cells: 10 Years On. *Cell*
780 *174*, 1054-1066. 10.1016/j.cell.2018.07.017.
- 781 2. Kotas, M.E., and Locksley, R.M. (2018). Why Innate Lymphoid Cells? *Immunity* *48*, 1081-1090.
782 10.1016/j.immuni.2018.06.002.
- 783 3. Diefenbach, A., Colonna, M., and Koyasu, S. (2014). Development, differentiation, and diversity
784 of innate lymphoid cells. *Immunity* *41*, 354-365. 10.1016/j.immuni.2014.09.005.
- 785 4. Klose, C.S.N., and Artis, D. (2016). Innate lymphoid cells as regulators of immunity,
786 inflammation and tissue homeostasis. *Nat Immunol* *17*, 765-774. 10.1038/ni.3489.
- 787 5. Spits, H., Bernink, J.H., and Lanier, L. (2016). NK cells and type 1 innate lymphoid cells:
788 partners in host defense. *Nat Immunol* *17*, 758-764. 10.1038/ni.3482.
- 789 6. Romero-Suarez, S., Del Rio Serrato, A., Bueno, R.J., Brunotte-Strecker, D., Stehle, C.,
790 Figueiredo, C.A., Hertwig, L., Dunay, I.R., Romagnani, C., and Infante-Duarte, C. (2019). The
791 Central Nervous System Contains ILC1s That Differ From NK Cells in the Response to
792 Inflammation. *Front Immunol* *10*, 2337. 10.3389/fimmu.2019.02337.
- 793 7. Vivier, E., Tomasello, E., Baratin, M., Walzer, T., and Ugolini, S. (2008). Functions of natural
794 killer cells. *Nat Immunol* *9*, 503-510. 10.1038/ni1582.
- 795 8. Saluzzo, S., Gorki, A.D., Rana, B.M.J., Martins, R., Scanlon, S., Starkl, P., Lakovits, K., Hladik,
796 A., Korosec, A., Sharif, O., et al. (2017). First-Breath-Induced Type 2 Pathways Shape the Lung
797 Immune Environment. *Cell Rep* *18*, 1893-1905. 10.1016/j.celrep.2017.01.071.
- 798 9. Schneider, C., Lee, J., Koga, S., Ricardo-Gonzalez, R.R., Nussbaum, J.C., Smith, L.K., Villeda,
799 S.A., Liang, H.E., and Locksley, R.M. (2019). Tissue-Resident Group 2 Innate Lymphoid Cells
800 Differentiate by Layered Ontogeny and In Situ Perinatal Priming. *Immunity* *50*, 1425-1438
801 e1425. 10.1016/j.immuni.2019.04.019.
- 802 10. Stehle, C., Ruckert, T., Fiancette, R., Gajdasik, D.W., Willis, C., Ulbricht, C., Durek, P.,
803 Mashreghi, M.F., Finke, D., Hauser, A.E., et al. (2021). T-bet and RORalpha control lymph
804 node formation by regulating embryonic innate lymphoid cell differentiation. *Nat Immunol* *22*,
805 1231-1244. 10.1038/s41590-021-01029-6.
- 806 11. Bando, J.K., Liang, H.E., and Locksley, R.M. (2015). Identification and distribution of developing
807 innate lymphoid cells in the fetal mouse intestine. *Nat Immunol* *16*, 153-160. 10.1038/ni.3057.
- 808 12. Hernandez-Torres, D.C., and Stehle, C. (2022). Embryonic ILC-poiesis across tissues. *Front*
809 *Immunol* *13*, 1040624. 10.3389/fimmu.2022.1040624.
- 810 13. Moro, K., Kabata, H., Tanabe, M., Koga, S., Takeno, N., Mochizuki, M., Fukunaga, K., Asano,
811 K., Betsuyaku, T., and Koyasu, S. (2016). Interferon and IL-27 antagonize the function of group
812 2 innate lymphoid cells and type 2 innate immune responses. *Nat Immunol* *17*, 76-86.
813 10.1038/ni.3309.
- 814 14. Gasteiger, G., Fan, X., Dikiy, S., Lee, S.Y., and Rudensky, A.Y. (2015). Tissue residency of
815 innate lymphoid cells in lymphoid and nonlymphoid organs. *Science* *350*, 981-985.
816 10.1126/science.aac9593.
- 817 15. Sparano, C., Solis-Sayago, D., Vijaykumar, A., Rickenbach, C., Vermeer, M., Ingelfinger, F.,
818 Litscher, G., Fonseca, A., Mussak, C., Mayoux, M., et al. (2022). Embryonic and neonatal
819 waves generate distinct populations of hepatic ILC1s. *Sci Immunol* *7*, eabo6641.
820 10.1126/sciimmunol.abo6641.
- 821 16. Simic, M., Manosalva, I., Spinelli, L., Gentek, R., Shayan, R.R., Siret, C., Girard-Madoux, M.,
822 Wang, S., de Fabritus, L., Verschoor, J., et al. (2020). Distinct Waves from the Hemogenic
823 Endothelium Give Rise to Layered Lymphoid Tissue Inducer Cell Ontogeny. *Cell Rep* *32*,
824 108004. 10.1016/j.celrep.2020.108004.
- 825 17. Kabil, A., Shin, S.B., Hughes, M.R., and McNagny, K.M. (2022). "Just one word, plastic!":
826 Controversies and caveats in innate lymphoid cell plasticity. *Front Immunol* *13*, 946905.
827 10.3389/fimmu.2022.946905.
- 828 18. Bal, S.M., Golebski, K., and Spits, H. (2020). Plasticity of innate lymphoid cell subsets. *Nat Rev*
829 *Immunol* *20*, 552-565. 10.1038/s41577-020-0282-9.
- 830 19. Bernink, J.H., Peters, C.P., Munneke, M., te Velde, A.A., Meijer, S.L., Weijer, K.,
831 Hreggvidsdottir, H.S., Heinsbroek, S.E., Legrand, N., Buskens, C.J., et al. (2013). Human type
832 1 innate lymphoid cells accumulate in inflamed mucosal tissues. *Nat Immunol* *14*, 221-229.
833 10.1038/ni.2534.
- 834 20. Klose, C.S., Kiss, E.A., Schwierzeck, V., Ebert, K., Hoyler, T., d'Hargues, Y., Goppert, N.,
835 Croxford, A.L., Waisman, A., Tanriver, Y., and Diefenbach, A. (2013). A T-bet gradient controls

- 836 the fate and function of CCR6-RORgammat+ innate lymphoid cells. *Nature* 494, 261-265.
837 10.1038/nature11813.
- 838 21. Vonarbourg, C., Mortha, A., Bui, V.L., Hernandez, P.P., Kiss, E.A., Hoyler, T., Flach, M.,
839 Bengsch, B., Thimme, R., Holscher, C., et al. (2010). Regulated expression of nuclear receptor
840 RORgammat confers distinct functional fates to NK cell receptor-expressing RORgammat(+)
841 innate lymphocytes. *Immunity* 33, 736-751. 10.1016/j.immuni.2010.10.017.
- 842 22. Verrier, T., Satoh-Takayama, N., Serafini, N., Marie, S., Di Santo, J.P., and Vosshenrich, C.A.
843 (2016). Phenotypic and Functional Plasticity of Murine Intestinal NKp46+ Group 3 Innate
844 Lymphoid Cells. *J Immunol* 196, 4731-4738. 10.4049/jimmunol.1502673.
- 845 23. Yudanin, N.A., Schmitz, F., Flamar, A.L., Thome, J.J.C., Tait Wojno, E., Moeller, J.B., Schirmer,
846 M., Latorre, I.J., Xavier, R.J., Farber, D.L., et al. (2019). Spatial and Temporal Mapping of
847 Human Innate Lymphoid Cells Reveals Elements of Tissue Specificity. *Immunity* 50, 505-519
848 e504. 10.1016/j.immuni.2019.01.012.
- 849 24. Korchagina, A.A., Koroleva, E., and Tumanov, A.V. (2023). Innate Lymphoid Cell Plasticity in
850 Mucosal Infections. *Microorganisms* 11. 10.3390/microorganisms11020461.
- 851 25. Golomb, S.M., Guldner, I.H., Zhao, A., Wang, Q., Palakurthi, B., Aleksandrovic, E.A., Lopez,
852 J.A., Lee, S.W., Yang, K., and Zhang, S. (2020). Multi-modal Single-Cell Analysis Reveals Brain
853 Immune Landscape Plasticity during Aging and Gut Microbiota Dysbiosis. *Cell Rep* 33, 108438.
854 10.1016/j.celrep.2020.108438.
- 855 26. Fung, I.T.H., Sankar, P., Zhang, Y., Robison, L.S., Zhao, X., D'Souza, S.S., Salinero, A.E.,
856 Wang, Y., Qian, J., Kuentzel, M.L., et al. (2020). Activation of group 2 innate lymphoid cells
857 alleviates aging-associated cognitive decline. *J Exp Med* 217. 10.1084/jem.20190915.
- 858 27. Yeung, S.S., Ho, Y.S., and Chang, R.C. (2021). The role of meningeal populations of type II
859 innate lymphoid cells in modulating neuroinflammation in neurodegenerative diseases. *Exp Mol*
860 *Med* 53, 1251-1267. 10.1038/s12276-021-00660-5.
- 861 28. Grigg, J.B., Shanmugavadivu, A., Regen, T., Parkhurst, C.N., Ahmed, A., Joseph, A.M.,
862 Mazzucco, M., Gronke, K., Diefenbach, A., Eberl, G., et al. (2021). Antigen-presenting innate
863 lymphoid cells orchestrate neuroinflammation. *Nature* 600, 707-712. 10.1038/s41586-021-
864 04136-4.
- 865 29. Kwong, B., Rua, R., Gao, Y., Flickinger, J., Jr., Wang, Y., Kruhlak, M.J., Zhu, J., Vivier, E.,
866 McGavern, D.B., and Lazarevic, V. (2017). T-bet-dependent NKp46(+) innate lymphoid cells
867 regulate the onset of T(H)17-induced neuroinflammation. *Nat Immunol* 18, 1117-1127.
868 10.1038/ni.3816.
- 869 30. Gadani, S.P., Smirnov, I., Wiltbank, A.T., Overall, C.C., and Kipnis, J. (2017). Characterization
870 of meningeal type 2 innate lymphocytes and their response to CNS injury. *J Exp Med* 214, 285-
871 296. 10.1084/jem.20161982.
- 872 31. Russi, A.E., Ebel, M.E., Yang, Y., and Brown, M.A. (2018). Male-specific IL-33 expression
873 regulates sex-dimorphic EAE susceptibility. *Proc Natl Acad Sci U S A* 115, E1520-E1529.
874 10.1073/pnas.1710401115.
- 875 32. Van Hove, H., Martens, L., Scheyltjens, I., De Vlaminck, K., Pombo Antunes, A.R., De Prijck,
876 S., Vandamme, N., De Schepper, S., Van Isterdael, G., Scott, C.L., et al. (2019). A single-cell
877 atlas of mouse brain macrophages reveals unique transcriptional identities shaped by ontogeny
878 and tissue environment. *Nat Neurosci* 22, 1021-1035. 10.1038/s41593-019-0393-4.
- 879 33. Steffen, J., Ehrentraut, S., Bank, U., Biswas, A., Figueiredo, C.A., Holsken, O., Dusedau, H.P.,
880 Dovhan, V., Knop, L., Thode, J., et al. (2022). Type 1 innate lymphoid cells regulate the onset
881 of *Toxoplasma gondii*-induced neuroinflammation. *Cell Rep* 38, 110564.
882 10.1016/j.celrep.2022.110564.
- 883 34. Ishizuka, I.E., Chea, S., Gudjonson, H., Constantinides, M.G., Dinner, A.R., Bendelac, A., and
884 Golub, R. (2016). Single-cell analysis defines the divergence between the innate lymphoid cell
885 lineage and lymphoid tissue-inducer cell lineage. *Nat Immunol* 17, 269-276. 10.1038/ni.3344.
- 886 35. Gogoleva, V.S., Kuprash, D.V., Grivennikov, S.I., Tumanov, A.V., Kruglov, A.A., and
887 Nedospasov, S.A. (2022). LTalpha, TNF, and ILC3 in Peyer's Patch Organogenesis. *Cells* 11.
888 10.3390/cells11121970.
- 889 36. Magliozzi, R., Columba-Cabezas, S., Serafini, B., and Aloisi, F. (2004). Intracerebral
890 expression of CXCL13 and BAFF is accompanied by formation of lymphoid follicle-like
891 structures in the meninges of mice with relapsing experimental autoimmune encephalomyelitis.
892 *J Neuroimmunol* 148, 11-23. 10.1016/j.jneuroim.2003.10.056.
- 893 37. Magliozzi, R., Howell, O., Vora, A., Serafini, B., Nicholas, R., Puopolo, M., Reynolds, R., and
894 Aloisi, F. (2007). Meningeal B-cell follicles in secondary progressive multiple sclerosis

- 895 associate with early onset of disease and severe cortical pathology. *Brain* 130, 1089-1104.
896 10.1093/brain/awm038.
- 897 38. Quintana, J.F., Sinton, M.C., Chandrasegaran, P., Kumar Dubey, L., Ogunsola, J., Al Samman,
898 M., Haley, M., McConnell, G., Kuispond Swar, N.R., Ngoyi, D.M., et al. (2023). The murine
899 meninges acquire lymphoid tissue properties and harbour autoreactive B cells during chronic
900 *Trypanosoma brucei* infection. *PLoS Biol* 21, e3002389. 10.1371/journal.pbio.3002389.
- 901 39. Izen, R.M., Yamazaki, T., Nishinaka-Arai, Y., Hong, Y.K., and Mukouyama, Y.S. (2018).
902 Postnatal development of lymphatic vasculature in the brain meninges. *Dev Dyn* 247, 741-753.
903 10.1002/dvdy.24624.
- 904 40. Alves de Lima, K., Rustenhoven, J., Da Mesquita, S., Wall, M., Salvador, A.F., Smirnov, I.,
905 Martelossi Cebinelli, G., Mamuladze, T., Baker, W., Papadopoulos, Z., et al. (2020). Meningeal
906 $\gamma\delta$ T cells regulate anxiety-like behavior via IL-17a signaling in neurons. *Nat Immunol* 21, 1421-
907 1429. 10.1038/s41590-020-0776-4.
- 908 41. Tanabe, S., and Yamashita, T. (2018). B-1a lymphocytes promote oligodendrogenesis during
909 brain development. *Nature Neuroscience* 21, 506-516. 10.1038/s41593-018-0106-4.
- 910 42. Si, Y., Zhang, Y., Zuloaga, K., and Yang, Q. (2023). The role of innate lymphocytes in regulating
911 brain and cognitive function. *Neurobiol Dis* 179, 106061. 10.1016/j.nbd.2023.106061.
- 912 43. Zeis, P., Lian, M., Fan, X., Herman, J.S., Hernandez, D.C., Gentek, R., Elias, S., Symowski,
913 C., Knopper, K., Peltokangas, N., et al. (2020). In Situ Maturation and Tissue Adaptation of
914 Type 2 Innate Lymphoid Cell Progenitors. *Immunity* 53, 775-792 e779.
915 10.1016/j.immuni.2020.09.002.
- 916 44. Ricardo-Gonzalez, R.R., Van Dyken, S.J., Schneider, C., Lee, J., Nussbaum, J.C., Liang, H.E.,
917 Vaka, D., Eckalbar, W.L., Molofsky, A.B., Erle, D.J., and Locksley, R.M. (2018). Tissue signals
918 imprint ILC2 identity with anticipatory function. *Nat Immunol* 19, 1093-1099. 10.1038/s41590-
919 018-0201-4.
- 920 45. Fantuzzi, L., Tagliamonte, M., Gauzzi, M.C., and Lopalco, L. (2019). Dual CCR5/CCR2
921 targeting: opportunities for the cure of complex disorders. *Cell Mol Life Sci* 76, 4869-4886.
922 10.1007/s00018-019-03255-6.
- 923 46. Ronaldson, P.T., and Davis, T.P. (2020). Regulation of blood-brain barrier integrity by microglia
924 in health and disease: A therapeutic opportunity. *J Cereb Blood Flow Metab* 40, S6-S24.
925 10.1177/0271678X20951995.
- 926 47. Zhao, M., Shao, F., Yu, D., Zhang, J., Liu, Z., Ma, J., Xia, P., and Wang, S. (2022). Maturation
927 and specialization of group 2 innate lymphoid cells through the lung-gut axis. *Nat Commun* 13,
928 7600. 10.1038/s41467-022-35347-6.
- 929 48. Dahlgren, M.W., Jones, S.W., Cautivo, K.M., Dubinin, A., Ortiz-Carpena, J.F., Farhat, S., Yu,
930 K.S., Lee, K., Wang, C., Molofsky, A.V., et al. (2019). Adventitial Stromal Cells Define Group 2
931 Innate Lymphoid Cell Tissue Niches. *Immunity* 50, 707-722 e706.
932 10.1016/j.immuni.2019.02.002.
- 933 49. Cautivo, K.M., Matatia, P.R., Lizama, C.O., Mroz, N.M., Dahlgren, M.W., Yu, X., Snierski-Kind,
934 J., Taruselli, M.T., Brooks, J.F., Wade-Vallance, A., et al. (2022). Interferon gamma constrains
935 type 2 lymphocyte niche boundaries during mixed inflammation. *Immunity* 55, 254-271 e257.
936 10.1016/j.immuni.2021.12.014.
- 937 50. Janzer, R.C., and Raff, M.C. (1987). Astrocytes induce blood-brain barrier properties in
938 endothelial cells. *Nature* 325, 253-257. 10.1038/325253a0.
- 939 51. Bauer, H.C., Bauer, H., Lametschwandtner, A., Amberger, A., Ruiz, P., and Steiner, M. (1993).
940 Neovascularization and the appearance of morphological characteristics of the blood-brain
941 barrier in the embryonic mouse central nervous system. *Brain Res Dev Brain Res* 75, 269-278.
942 10.1016/0165-3806(93)90031-5.
- 943 52. Robinette, M.L., Bando, J.K., Song, W., Ulland, T.K., Gilfillan, S., and Colonna, M. (2017). IL-
944 15 sustains IL-7R-independent ILC2 and ILC3 development. *Nat Commun* 8, 14601.
945 10.1038/ncomms14601.
- 946 53. O'Sullivan, T.E., Geary, C.D., Weizman, O.E., Geiger, T.L., Rapp, M., Dorn, G.W., 2nd,
947 Overholtzer, M., and Sun, J.C. (2016). *Atg5* Is Essential for the Development and Survival of
948 Innate Lymphocytes. *Cell Rep* 15, 1910-1919. 10.1016/j.celrep.2016.04.082.
- 949 54. Jones, R., Cosway, E.J., Willis, C., White, A.J., Jenkinson, W.E., Fehling, H.J., Anderson, G.,
950 and Withers, D.R. (2018). Dynamic changes in intrathymic ILC populations during murine
951 neonatal development. *Eur J Immunol* 48, 1481-1491. 10.1002/eji.201847511.
- 952 55. Bernink, J.H., Krabbendam, L., Germar, K., de Jong, E., Gronke, K., Kofoed-Nielsen, M.,
953 Munneke, J.M., Hazenberg, M.D., Villaudy, J., Buskens, C.J., et al. (2015). Interleukin-12 and

- 954 -23 Control Plasticity of CD127(+) Group 1 and Group 3 Innate Lymphoid Cells in the Intestinal
955 Lamina Propria. *Immunity* 43, 146-160. 10.1016/j.immuni.2015.06.019.
- 956 56. Mikami, Y., Scarno, G., Zitti, B., Shih, H.Y., Kanno, Y., Santoni, A., O'Shea, J.J., and Sciume,
957 G. (2018). NCR(+) ILC3 maintain larger STAT4 reservoir via T-BET to regulate type 1 features
958 upon IL-23 stimulation in mice. *Eur J Immunol* 48, 1174-1180. 10.1002/eji.201847480.
- 959 57. Krzywinska, E., Sobocki, M., Nagarajan, S., Zacharjasz, J., Tambuwala, M.M., Pelletier, A.,
960 Cummins, E., Gotthardt, D., Fandrey, J., Kerdiles, Y.M., et al. (2022). The transcription factor
961 HIF-1 α mediates plasticity of NKp46+ innate lymphoid cells in the gut. *J Exp Med* 219.
962 10.1084/jem.20210909.
- 963 58. Nayar, S., Campos, J., Chung, M.M., Navarro-Nunez, L., Chachlani, M., Steinthal, N., Gardner,
964 D.H., Rankin, P., Cloake, T., Caamano, J.H., et al. (2016). Bimodal Expansion of the Lymphatic
965 Vessels Is Regulated by the Sequential Expression of IL-7 and Lymphotoxin α 1 β 2 in
966 Newly Formed Tertiary Lymphoid Structures. *J Immunol* 197, 1957-1967.
967 10.4049/jimmunol.1500686.
- 968 59. Furtado, G.C., Pacer, M.E., Bongers, G., Benezech, C., He, Z., Chen, L., Berin, M.C., Kollias,
969 G., Caamano, J.H., and Lira, S.A. (2014). TNF α -dependent development of lymphoid
970 tissue in the absence of ROR γ t(+) lymphoid tissue inducer cells. *Mucosal Immunol* 7,
971 602-614. 10.1038/mi.2013.79.
- 972 60. Louveau, A., Smirnov, I., Keyes, T.J., Eccles, J.D., Rouhani, S.J., Peske, J.D., Derecki, N.C.,
973 Castle, D., Mandell, J.W., Lee, K.S., et al. (2015). Structural and functional features of central
974 nervous system lymphatic vessels. *Nature* 523, 337-341. 10.1038/nature14432.
- 975 61. Li, Z., Antila, S., Nurmi, H., Chilov, D., Korhonen, E.A., Fang, S., Karaman, S., Engelhardt, B.,
976 and Alitalo, K. (2023). Blockade of VEGFR3 signaling leads to functional impairment of dural
977 lymphatic vessels without affecting autoimmune neuroinflammation. *Sci Immunol* 8, eabq0375.
978 10.1126/sciimmunol.abq0375.
- 979 62. Ji, H., Cao, R., Yang, Y., Zhang, Y., Iwamoto, H., Lim, S., Nakamura, M., Andersson, P., Wang,
980 J., Sun, Y., et al. (2014). TNFR1 mediates TNF- α -induced tumour lymphangiogenesis and
981 metastasis by modulating VEGF-C-VEGFR3 signalling. *Nat Commun* 5, 4944.
982 10.1038/ncomms5944.
- 983 63. Eberl, G., Marmon, S., Sunshine, M.J., Rennert, P.D., Choi, Y., and Littman, D.R. (2004). An
984 essential function for the nuclear receptor ROR γ t in the generation of fetal lymphoid
985 tissue inducer cells. *Nat Immunol* 5, 64-73. 10.1038/ni1022.
- 986 64. Rawlins, E.L., Clark, C.P., Xue, Y., and Hogan, B.L. (2009). The Id2+ distal tip lung epithelium
987 contains individual multipotent embryonic progenitor cells. *Development* 136, 3741-3745.
988 10.1242/dev.037317.
- 989 65. Mombaerts, P., Iacomini, J., Johnson, R.S., Herrup, K., Tonegawa, S., and Papaioannou, V.E.
990 (1992). RAG-1-deficient mice have no mature B and T lymphocytes. *Cell* 68, 869-877.
991 10.1016/0092-8674(92)90030-g.
- 992 66. Srinivas, S., Watanabe, T., Lin, C.S., Williams, C.M., Tanabe, Y., Jessell, T.M., and Costantini,
993 F. (2001). Cre reporter strains produced by targeted insertion of EYFP and ECFP into the
994 ROSA26 locus. *BMC Dev Biol* 1, 4. 10.1186/1471-213x-1-4.
- 995 67. Muraro, M.J., Dharmadhikari, G., Grun, D., Groen, N., Dielen, T., Jansen, E., van Gorp, L.,
996 Engelse, M.A., Carlotti, F., de Koning, E.J., and van Oudenaarden, A. (2016). A Single-Cell
997 Transcriptome Atlas of the Human Pancreas. *Cell Syst* 3, 385-394 e383.
998 10.1016/j.cels.2016.09.002.
- 999 68. van den Brink, S.C., Sage, F., Vertesy, A., Spanjaard, B., Peterson-Maduro, J., Baron, C.S.,
1000 Robin, C., and van Oudenaarden, A. (2017). Single-cell sequencing reveals dissociation-
1001 induced gene expression in tissue subpopulations. *Nat Methods* 14, 935-936.
1002 10.1038/nmeth.4437.
- 1003 69. Hashimshony, T., Senderovich, N., Avital, G., Klochendler, A., de Leeuw, Y., Anavy, L.,
1004 Gennert, D., Li, S., Livak, K.J., Rozenblatt-Rosen, O., et al. (2016). CEL-Seq2: sensitive highly-
1005 multiplexed single-cell RNA-Seq. *Genome Biol* 17, 77. 10.1186/s13059-016-0938-8.
- 1006 70. Denisenko, E., Guo, B.B., Jones, M., Hou, R., de Kock, L., Lassmann, T., Poppe, D., Clement,
1007 O., Simmons, R.K., Lister, R., and Forrest, A.R.R. (2020). Systematic assessment of tissue
1008 dissociation and storage biases in single-cell and single-nucleus RNA-seq workflows. *Genome*
1009 *Biol* 21, 130. 10.1186/s13059-020-02048-6.
- 1010 71. Wu, T., Hu, E., Xu, S., Chen, M., Guo, P., Dai, Z., Feng, T., Zhou, L., Tang, W., Zhan, L., et al.
1011 (2021). clusterProfiler 4.0: A universal enrichment tool for interpreting omics data. *Innovation*
1012 (Camb) 2, 100141. 10.1016/j.xinn.2021.100141.

- 1013 72. Korotkevich, G., Sukhov, V., Budin, N., Shpak, B., Artyomov, M.N., and Sergushichev, A.
1014 (2021). Fast gene set enrichment analysis. *bioRxiv*, 060012. 10.1101/060012.
1015 73. Trapnell, C., Cacchiarelli, D., Grimsby, J., Pokharel, P., Li, S., Morse, M., Lennon, N.J., Livak,
1016 K.J., Mikkelsen, T.S., and Rinn, J.L. (2014). The dynamics and regulators of cell fate decisions
1017 are revealed by pseudotemporal ordering of single cells. *Nat Biotechnol* 32, 381-386.
1018 10.1038/nbt.2859.
1019 74. Cao, J., Packer, J.S., Ramani, V., Cusanovich, D.A., Huynh, C., Daza, R., Qiu, X., Lee, C.,
1020 Furlan, S.N., Steemers, F.J., et al. (2017). Comprehensive single-cell transcriptional profiling
1021 of a multicellular organism. *Science* 357, 661-667. 10.1126/science.aam8940.
1022

1023

1024 **Data availability**

1025 The authors declare that the data supporting these findings are present in the paper or the
1026 Supplementary Materials. Raw data are available from the authors upon reasonable request.
1027 RNA sequencing data will be available through GEO #[submission in progress].

1028

1029 **Author contribution**

1030 A.D.R.S. designed the study, performed the experiments with the help of B.L.H. and E.V.,
1031 analyzed the data, prepared the figures, and wrote the manuscript. C.S., O.H., A.D., and C.R.
1032 provided technical and conceptual advice and relevant resources. CI-D. designed and directed
1033 the study and wrote the manuscript. All authors fully qualify for authorship and have approved
1034 the final version of the manuscript.

1035

1036 **Ethics declaration**

1037 The animal study was reviewed and approved by Berlin State Office for Health and Social
1038 Affairs (LAGeSo), Berlin, Germany.

1039

1040 **Conflict of interest**

1041 The authors declare that the research was conducted in the absence of any commercial or
1042 financial relationships that could be construed as a potential conflict of interest.

1043

1044 **Acknowledgement**

1045 We thank all the members of the Infante-Duarte lab for their helpful experimental advice and
1046 discussions. We especially thank Natascha Asselborn for all her technical assistance and
1047 Thordis Hohnstein with her support establishing the new transgenic animal lines in our
1048 breeding barrier. We also thank Single Cell Discoveries for their help with single cell
1049 sequencing services. In addition, we would like to thank Franke Vedran for his expert advice
1050 and guidance during the analysis of the single cell sequencing data. We would like to also
1051 acknowledge Caroline Braeuning from the BIH/MDC Genomics Technology Platform for her
1052 expert technical assistance and services in our FACS sorting experiments. We thank the

1053 Advanced Medical BioImaging Core Facility of the Charité-Universitätsmedizin Berlin (AMBIO)
1054 for support in acquisition of our imaging data and the Research Institute for Experimental
1055 Medicine (FEM) of the Charité (Berlin, Germany) for their excellent maintenance of our animal
1056 colonies and for the careful control of our breeding to provide us with animals along all the
1057 developmental timepoints studied in this paper. This study was funded by the German
1058 Research Foundation (Deutsche Forschungsgemeinschaft, DFG), Projekt Nr. 534335032,
1059 Grant ID: IN 156/8-1, and by the Hertie Foundation (GHS, Gemeinnützige Hertie-Stiftung),
1060 through the Hertie Network of Excellence in Clinical Neuroscience (Project Nr. P1200003).
1061 CID was also supported by the DFG-funded SFB1340-2, Grant Nr. 372486779, Project B05.

1062
1063
1064
1065
1066
1067
1068
1069
1070
1071
1072
1073
1074
1075
1076
1077
1078
1079
1080
1081
1082
1083
1084
1085
1086
1087
1088
1089

1090 **Figure legends**

1091

1092 **Figure 1. Young adult CNS harbors quiescent tissue-resident group 1 ILCs, ILC2s and**
1093 **ex-ILC3s.** Flow cytometry analysis of young adult C57BL/6J (WT) 8-11 weeks old (8-10wo)
1094 mice. **(A)** Gating strategy to identify ILCs as CD45^{high}Lin^{LD}CD3⁻NKp46⁺ and/or CD127⁺ cells,
1095 whose subset identity is confirmed by the expression of the lineage-associated TF ROR γ t,
1096 Eomes, T-bet or Gata3, that defined ILC3s, group 1 ILCs and ILC2s, respectively. **(B)** Uniform
1097 Manifold Approximation and Projection (UMAP) visualization of scRNA-seq of ILC clusters
1098 found within the total CD45⁺ immune cells isolated from the whole brain or microdissected
1099 border regions (dura mater and choroid plexus) of 9-week-old C57BL/6 mice. Each colored
1100 cluster identifies a subset of ILC1-like, NK and ILC2s (above) or CNS-compartment of origin
1101 (below). Data are from Van Hove et al., (2019). **(C)** Representative histograms of markers
1102 expression by each identified ILC subset from young adult CNS. **(D)** Quantification of the
1103 percentage of total ILCs within CD45^{high} cells and their absolute numbers **(E)** in whole brain
1104 (with leptomeninges and choroid plexus), spinal cord parenchyma (SC.P) and dura mater
1105 (D.M) of male and female young adults (8-10wo). Data depicted as mean \pm SEM., n = 8
1106 examined over \geq 3 independent experiments. D.M samples were pooled from two animals
1107 when necessary. **(F)** Absolute numbers of total ILCs in brain parenchyma (B.P, inc.
1108 leptomeninges), SC.P, choroid plexus (Ch.P) and D.M. Data depicted as mean \pm SEM., n = 4-
1109 10 examined over \geq 3 independent experiments. D.M and Ch.P samples were pooled from two
1110 animals if needed. ILC subgroups **(G)** frequency and **(H)** absolute counts in B.P, Ch.P and
1111 D.M were compared to peripheral blood (P.B). Data are shown as mean \pm SEM., n = 8-10
1112 examined over \geq 3 independent experiments. Dura meninges and choroid plexus samples
1113 were pooled from two animals when necessary. **(I)** Quantification of Ki67 expression among
1114 ILCs within the different CNS compartments. Data are depicted as mean \pm SEM., n = 6. **(J)**
1115 Mice were intravenously injected with anti-CD45-PE (2 mg) 3 minutes before euthanasia and
1116 perfusion. On the left, the representative gating for identification i.v. CD45-PE⁺ immune cells
1117 (CD45-PerCP⁺) in peripheral blood and brain parenchyma with the quantification depicted as
1118 mean \pm SD. The graph depicts the proportion of i.v. (intravascular) CD45⁺ cells among each
1119 ILC subset per compartment. Graph is depicted as mean \pm SEM., n = 4 examined over 2
1120 independent experiments. **(K)** Representative gating strategy for the identification of ILC3s
1121 and ex-ILC3s using the Rorc(gt)^{cre/wt} \times R26^{eYFP} fate map (FM)⁺ mice 2–3-month-old.

1122

1123 **Figure 2. ILCs start infiltrating the brain prenatally as progenitors and committed ILCs.**
1124 Flow cytometry analysis of E14 and E16 Id2^{GFP/+} reporter (indicated when used) and WT mice.
1125 Whole litters were pooled for each independent experiment. Analysis of Id2^{GFP/+} reporter

1126 animals includes WT and reporter animals within the pooled embryos. Of note, the rest of this
1127 study was always done in whole brain (inc. brain parenchyma, choroid plexus, leptomeningeal
1128 layers) and dura meninges was only analyzed separately when isolation was possible. **(A)**
1129 Representative gating of E16 Id2^{GFP/+} brain for identification of embryonic ILCs as
1130 CD45^{high}LinLD⁻CD3⁻CD122⁺ and/or CD127⁺ cells whose identity is confirmed by the
1131 expression of Id2-GFP. **(B)** Quantification and representative flow cytometry of GFP⁺CD122⁺
1132 and/or GFP⁺CD127⁺ ILCs from CD45⁺LinLD⁻CD3⁻ cells that start seeding the brain between
1133 E14 and E16 (n = 3 / timepoint). **(C)** Representative histograms of markers expression by
1134 CD122⁺CD127⁻ (P1), CD122⁻CD127⁺ (P3) and CD122⁺CD127⁺ (P2) populations from WT E16
1135 brain (n = 2-6). Control population (Ctrl. pop.) used for CD5 defined as CD45^{high}LinLD⁻CD3⁺.
1136 **(D)** Representative flow cytometry (left) of PD-1 and PLZF expression in CD45^{high}LinLD⁻CD3⁻
1137 CD122⁺ and/or CD127⁺ cells (total ILCs) and in P1, P2 and P3 (middle) from WT E16 brain.
1138 On the right, the quantification of these cells from the brain is depicted as mean ± SEM., n =
1139 5-8 examined over > 3 independent experiments. **(E)** Representative histograms of TF
1140 expression measurement of PD-1⁺PLZF⁺CD122⁺CD127⁺ (ILCp) from WT E16 brains (left).
1141 Graphs (right) show the mean fluorescence intensity (MFI) ± SEM for each TF in ILCp
1142 compared to the rest of the cells in P1, P2 and P3 (n = 4-8). Data are representative of ≥ 3
1143 independent experiments.

1144

1145 **Figure 3. The CNS ILC pool formation is mediated by subset specific dynamics of tissue**
1146 **seeding. (A)** Representative gating for the identification of the different ILC subsets in WT
1147 E16 whole brain: RORγt⁺ ILC3s, CD90.2⁺Gata3⁺ ILC2s and CD122⁺T-bet⁺ group 1 ILCs. The
1148 histogram representation along ontogeny of the CD122⁻CD127⁻ gate is depicted below. **(B)**
1149 ILC/T cell ratio over time in brain ontogeny (n = 3-7 / timepoint). **(C)** Absolute numbers of total
1150 ILCs (CD45⁺LinLD⁻CD3⁻CD127⁺ and/or CD122⁺) per gram of brain (n= 3-7/timepoint). **(D)**
1151 Frequencies of group 1 ILCs, ILC2s and ILC3s along brain ontogeny (n = 3-7 / timepoint). **(E)**
1152 Absolute numbers of each ILC subset in whole brain and **(F)** peripheral blood (n = 6-7 /
1153 timepoint). **(G)** Representative flow cytometry (left) and quantification (right) of Ki67
1154 expression in each ILC subset in brain along ontogeny (n = 3-7 / timepoint). From E16 to P1,
1155 whole litter were pooled. From P9 to P15 onwards, 2-3 animals were pooled if needed. Blood
1156 was sampled from heart puncture with volumes: E16: ~10 ul/animal, E18: ~15 ul/animal, P1:
1157 ~20 ul/animal, P9: ~50 ul/animal, P15: ~100 ul/animal, 5W: ~300 ul/animal.

1158

1159 **Figure 4. Single cell transcriptome profiling of newborn whole brain and dura cells**
1160 **shows a heterogeneous pool of mature ILCs. (A)** Representative gating strategy for the
1161 identification of fate map (FM)⁺ ex-vivo RORγt⁺ ILC3s in P9 Rorc(gt)^{cre/wt}×R26^{eYFP} mice (left)
1162 and quantification of YFP⁺RORγt⁺ ILC3s among CD45⁺LinLD⁻CD3⁻ cells depicted as

1163 mean \pm SEM., n = 2-5 / timepoint from ≥ 2 independent experiments. At P1 FM⁺ pups from the
1164 litter were pooled. From P9 onwards animals were analyzed individually. **(B)** Schematic
1165 representation of the experimental set-up used to sort live CD45⁺LinLD (Fixable Viability Dye,
1166 CD19, B220, Cd11b, Cd11c, Gr-1, F4/80, Fc ϵ R1 α)CD3⁻CD5⁻ cells expressing CD127 and/or
1167 CD122 from brain and dura meninges, isolated from C57BL/6J P9.5 mice. Cells were single-
1168 cell sequenced by an adapted version of the SORT-seq protocol⁶⁷. **(C)** UMAP depicted five
1169 distinct clusters along brain and dura meninges. **(D)** Gene expression UMAP plots of main
1170 subset-specific lineage markers. **(E)** Quantification of the frequency of ILC subsets identified
1171 by scRNA-seq and flow cytometry (FC) from total ILCs in brain and dura mater. For FC,
1172 percentages are shown as mean \pm SEM., n = 4-6. **(F)** Dot plot depicting selected gene
1173 expression (average and percentage) within clusters. **(G)** Transcriptional analysis of helper-
1174 like ILCs (ILC1s, ILC2s and ILC3s), excluding NK and proliferating cells. Heatmap
1175 representing average gene expression levels of ILC-homing receptor, chemokines,
1176 neurotransmitter, and other receptors within ILC clusters in whole brain and dura mater.

1177

1178 **Figure 5. Postnatal ILC3s show high survival but low proliferation capacity.** (A) Plot of
1179 the top pathways obtained by functional analysis on marker genes of cluster 2 (ILC3s) using
1180 the Hallmark pathway database. Bars represent the $-\log_{10}$ of the adjusted p values. **(B)** Dot
1181 plot depicting selected gene expression (average and percentage) of apoptosis and
1182 autophagy related markers within the identified clusters. **(C)** Representative flow cytometry
1183 plots of ILC1s (CD45⁺LinLD⁻CD3⁻NKp46⁺T-bet⁺Eomes⁻) and ILC3s (CD45⁺LinLD⁻CD3⁻
1184 ROR γ t⁺). Histograms show expression of Bcl-2 and Bim in ILC1 (blue line) and ILC3s (green
1185 line) together with isotype controls (black dashed lines). Quantification of the expression ratio
1186 between Bcl-2 and Bim in the different populations. Ratios are shown as mean \pm SEM, n = 6.
1187 Statistical test used is Mann-Whitney U test, **<0.01. **(D)** UMAP representation labeled by
1188 cell cycle phase. **(E)** Dot plot representation of the ILC-specific TFs among cluster 4
1189 (proliferating cells). **(F)** Quantification by flow cytometry of the percentage of Ki67 expressing
1190 cells among ILC-subtypes in brain and dura mater. Percentages are shown as mean \pm SEM.,
1191 n = 4-6. Statistical test used is Mann-Whitney U test, **<0.01.

1192 **Figure 6. A heterogeneous pool of ILC3s is present perinatally and undergo ILC3>ILC1**
1193 **conversion.** **(A)** Representative plots of the expression of CD4, NKp46 or CCR6 by ROR γ t⁺
1194 ILC3s along ontogeny. Mean frequencies are depicted in the graph. **(B)** UMAP dimensional
1195 reduction projection of ILC1/ILC3 superclusters reveals four separate subclusters. **(C)** Plot of
1196 the top pathways obtained by functional analysis on marker genes of cluster 1 (NKp46⁺-
1197 ILC3s) and cluster 2 (LTi) using the gene ontology biological process (BP), molecular function
1198 (MF) and cellular component (CC) databases. Bars represent the $-\log_{10}$ of the adjusted p
1199 values. **(D)** Trajectory analysis using Monocle 3 with origin cluster 1. Color-coded by cell

1200 distribution along pseudotime. **(E)** UMAP plots of the expression of the top genes driving the
1201 trajectory analysis projection. **(F)** Representative gating strategy for the identification of FM⁺
1202 ex-ILC3 in P9 and 10W Rorc(gt)^{cre/wt}×R26^{eYFP} mice (left) and quantification of YFP⁺ ex-ILC3s
1203 and double-positive RORgt⁺Tbet⁺ cells among Tbet⁺ ILCs depicted as mean ± SEM., n = 2-5 /
1204 timepoint from ≥ 2 independent experiments. From E16 to P1 whole litter were pooled. From
1205 P9 to P15 onwards, 2-3 animals were pooled if needed.

1206

1207 **Figure 7. Regional differences are present between perinatal brain and dura ILCs.**

1208 Transcriptional analysis of helper-like ILCs (ILC1s, ILC2s and ILC3s), excluding NK and
1209 proliferating cells. **(A)** Differential gene expression of ILC subsets in the brain and dura shown
1210 in a Volcano plot. Statistical analysis was performed by using non-parametric Wilcoxon rank
1211 sum. Red dots represent the genes highly expressed in brain, and blue dots represent the
1212 genes highly expressed in dura. **(B)** Results of GSEA GO biological process analysis showing
1213 enriched gene sets in brain vs. dura ILCs. The color in the bars indicate p adjusted values. A
1214 positive Normalized Enrichment Score (NES) value indicates enrichment in brain. A negative
1215 NES indicates enrichment in dura. **(C)** Heatmap of the DEGs for each ILC subtype in brain vs.
1216 dura selected based on Fisher p values < 0.05, resulted when performing Fisher exact P value
1217 test between single cell based non-parametric Wilcoxon rank test analysis and pseudobulk-
1218 based analysis using *ImFit*, *eBayes* and *topTable*. Expression values are represented as
1219 colors and range from red (high expression in brain), white (equal expression) and blue (high
1220 expression in dura). **(D)** Results of Hallmark analysis of identified differentially expressed
1221 genes in brain and the dura. The color depicts the p values meanwhile the bar size represents
1222 the k/K values of each pathway (ratio of number of DEGs divided by the number of genes in
1223 the indicated dataset).

1224

1225 **Figure 8. Altered lymphatic phenotype in the absence of RORgt⁺ ILCs but not Rag1^{-/-}.**

1226 **(A)** Representative plots (left) and quantification (right) of the expression of IL-17a, IL-22, INFg
1227 and TNFa among total brain RORyt⁺ ILC3s (n = 4-5) after stimulation with PMA/Ionomycin in
1228 the presence of Brefeldin A. Data are depicted as mean ± SEM. Data are representative of ≥
1229 3 independent experiments. Whole litter was always pooled for this analysis. **(B)**
1230 Representative images of Lyve-1-stained whole mount dura meninges showing lymphatic
1231 vessels located within the transversal sinus (TS) and the superior sagittal sinus (SS) (scale
1232 bar, 1000 μm). Square insets, higher magnification of Lyve-1, podoplanin and CD31 staining
1233 along the TS. **(C)** Representative images of control C57BL/6J, Rorgt-knockout (RORgt^{GFP/GFP})
1234 and T cell knockout (Rag1^{-/-}) dura meninges collected and stained for lyve-1 (scale bar, 1000
1235 μm). **(D)** Bar dot plots represent the ratio of the measurement of the Lyve-1 MFI staining along
1236 the TS and SSS between each knockout animal and its corresponding control C57BL/6J which

1237 was always analyzed in parallel. Ratios are shown as mean \pm SEM., n = 4-7. Statistical test
1238 used is Mann-Whitney U test. **(E)** Expression of lymphatic-associated markers determined by
1239 RT-qPCR in the dura of C57BL/6J mice (controls), ILC3 deficient (RORgt^{GFP/GFP}) and T cell
1240 deficient (Rag1^{-/-}) mice. Relative quantification normalized to control animals is shown as
1241 mean \pm SEM., n = 5-6. Statistical test used is Kruskal-Wallis test for three group comparison
1242 and Mann-Whitney U test for two group comparisons (* < 0.05; ** <0.01).

1243

1244

1245

1246

1247

1248

1249

1250

1251

1252

1253

1254

1255

1256

1257

1258

1259

1260

1261

1262

1263

1264

1265

1266

1267

1268

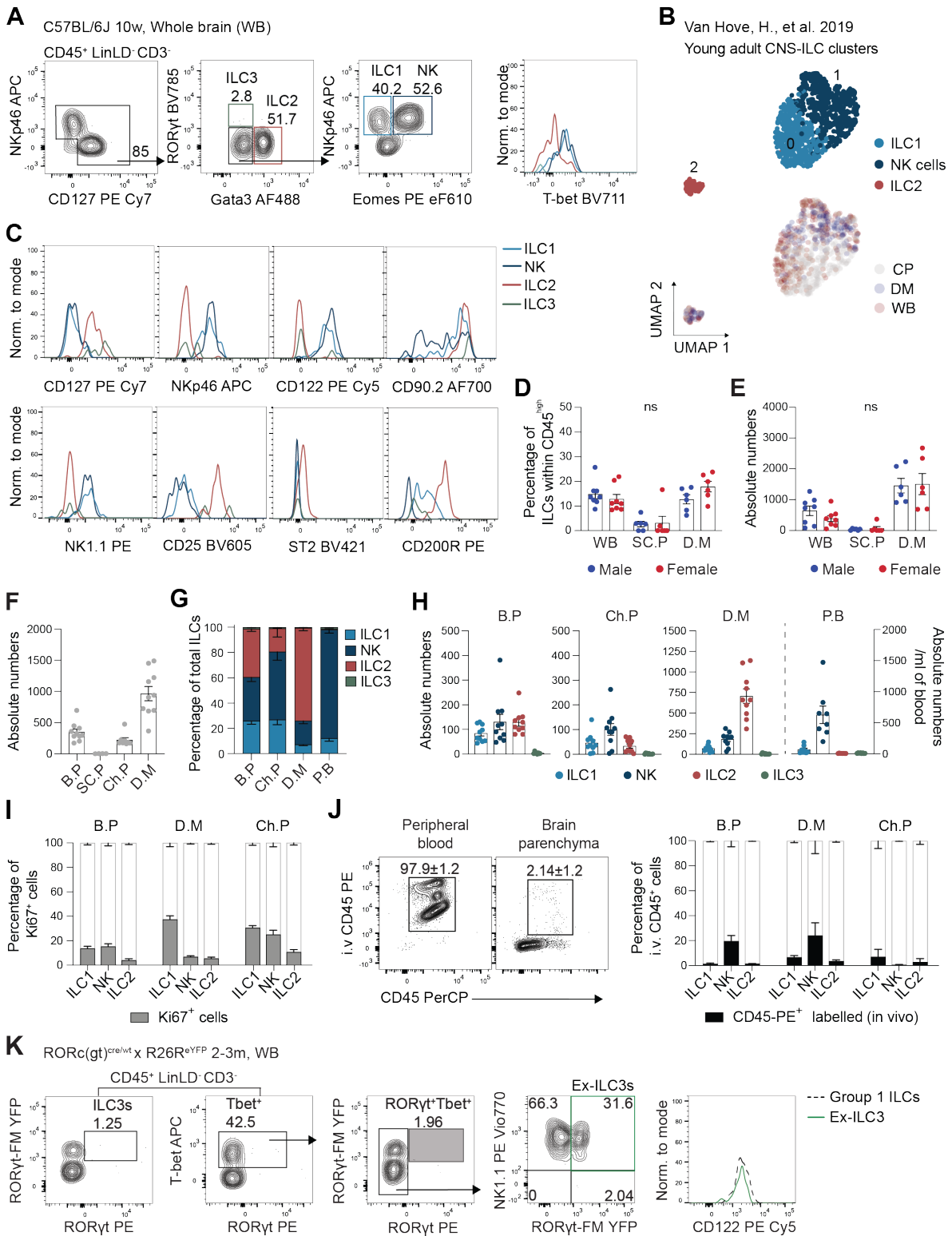
1269

1270

1271 **Figures**

1272

1273 **Figure 1**

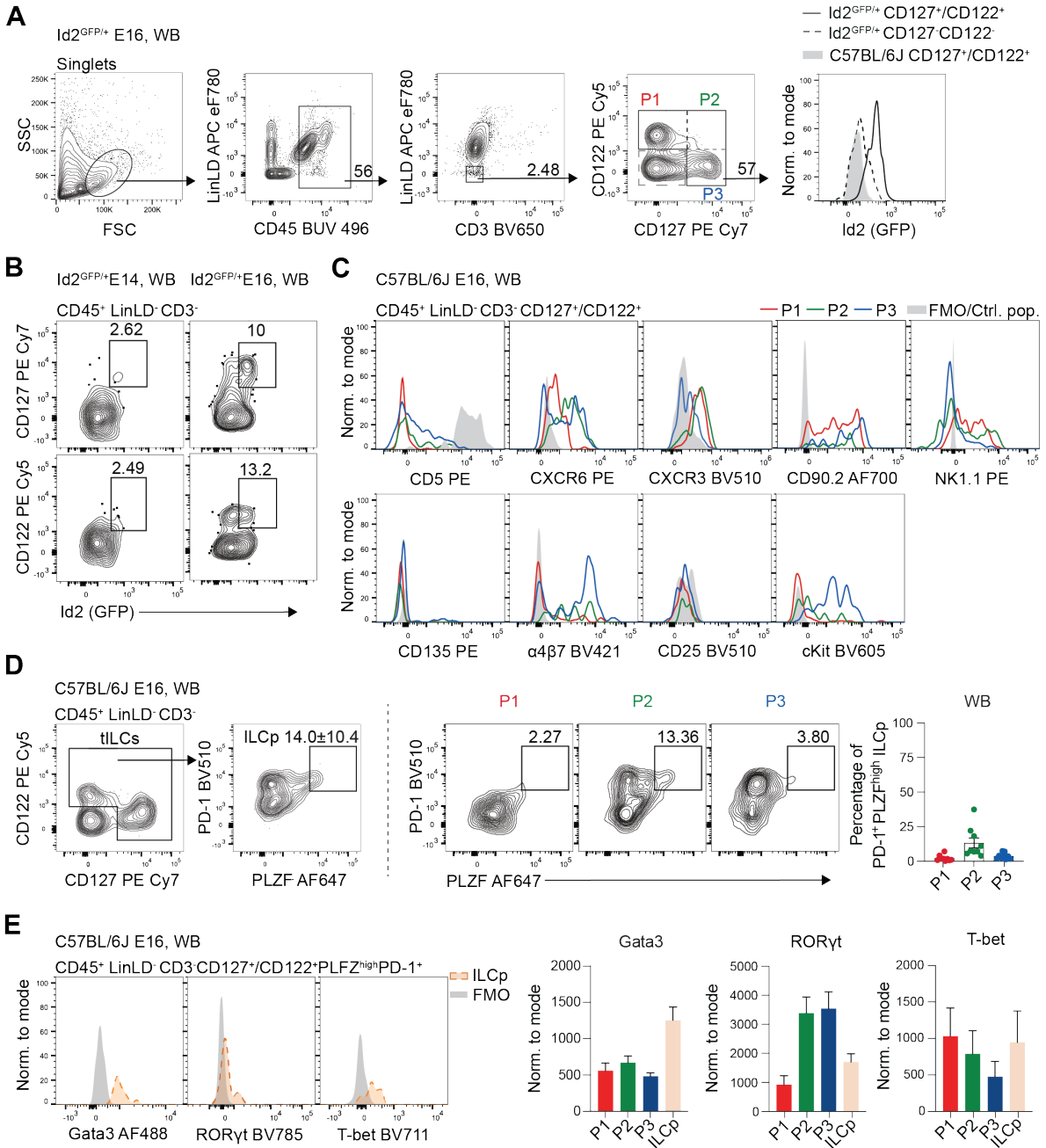


1274

1275

1276

1277 Figure 2



1278

1279

1280

1281

1282

1283

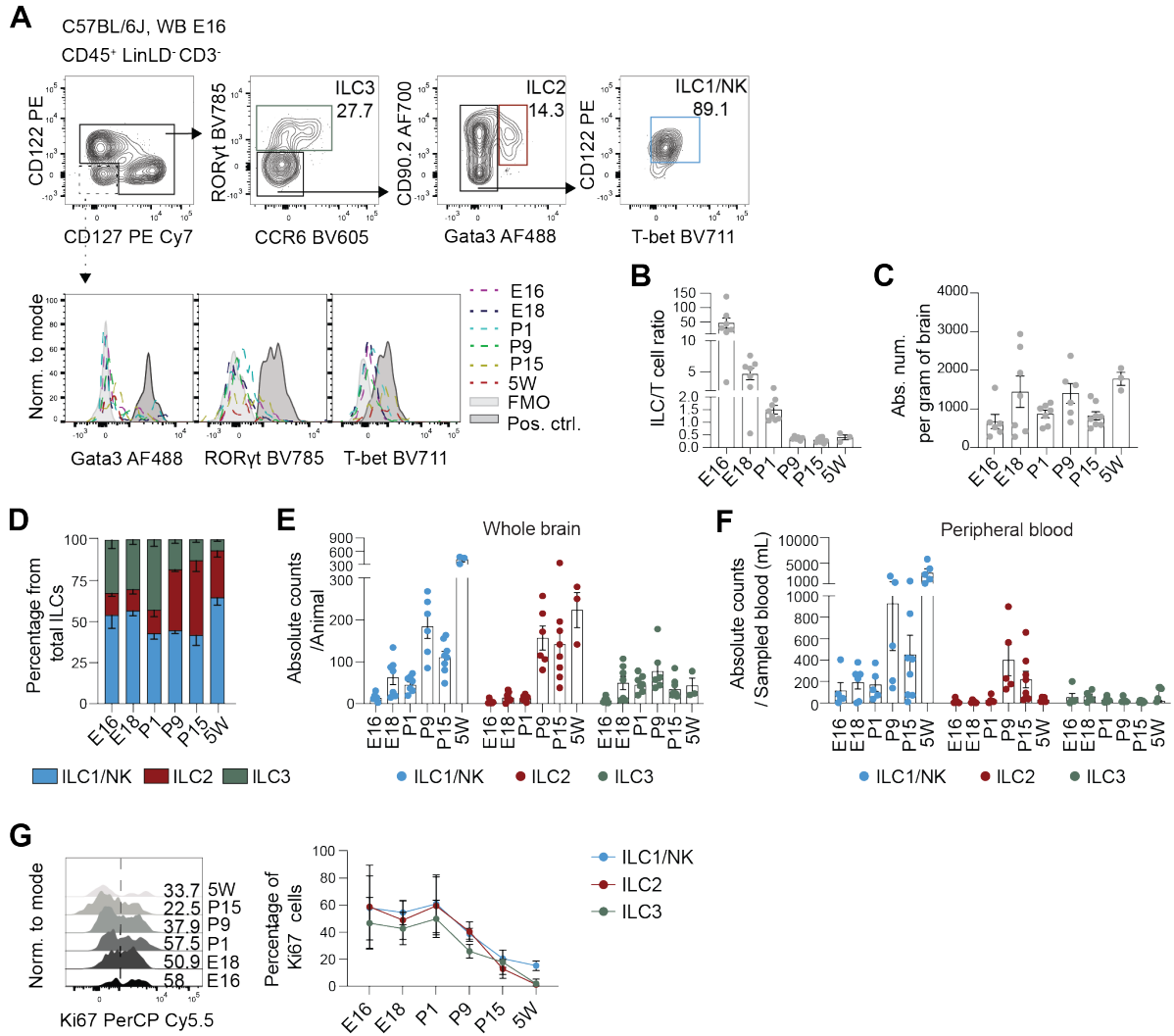
1284

1285

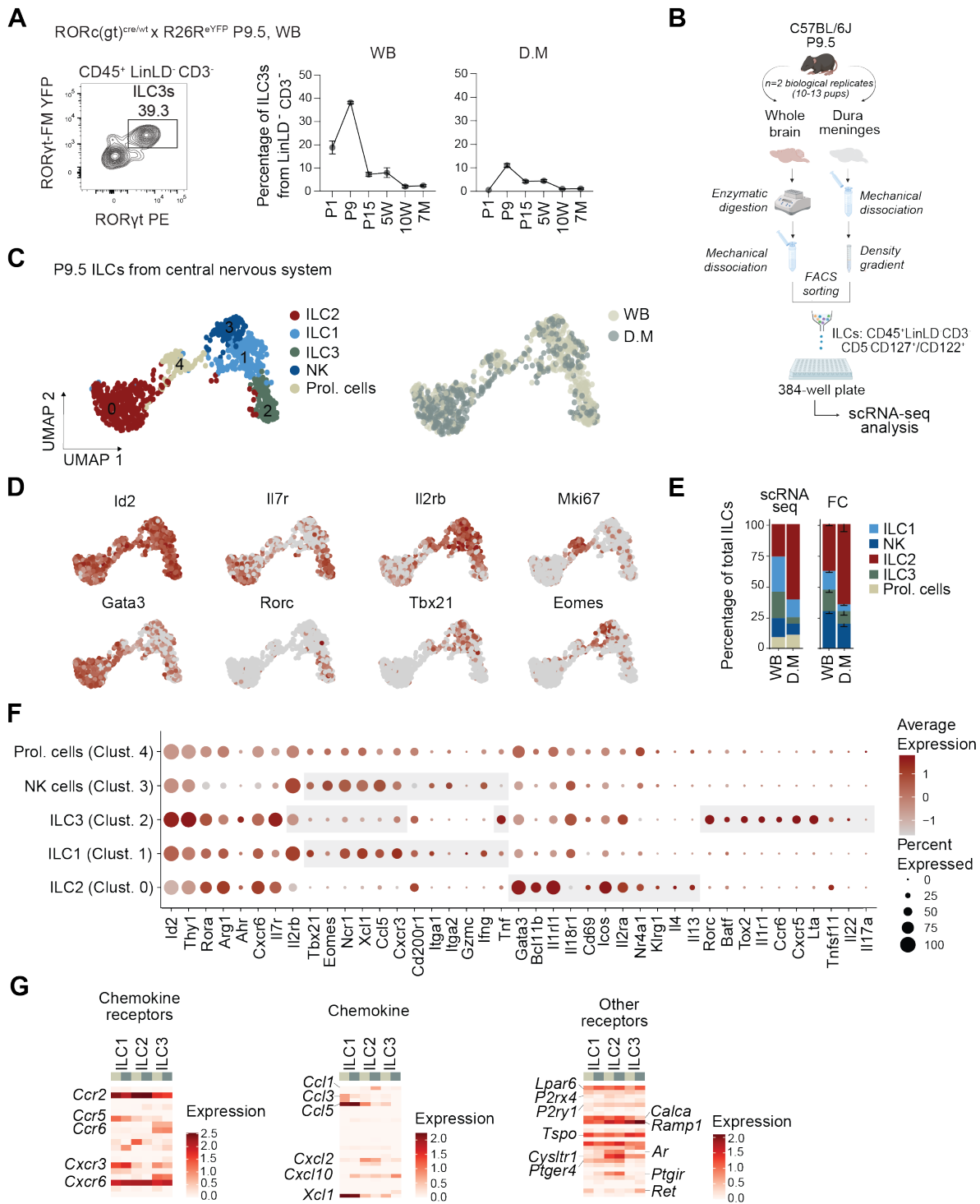
1286

1287

1288 Figure 3



1291 Figure 4



1292

1293

1294

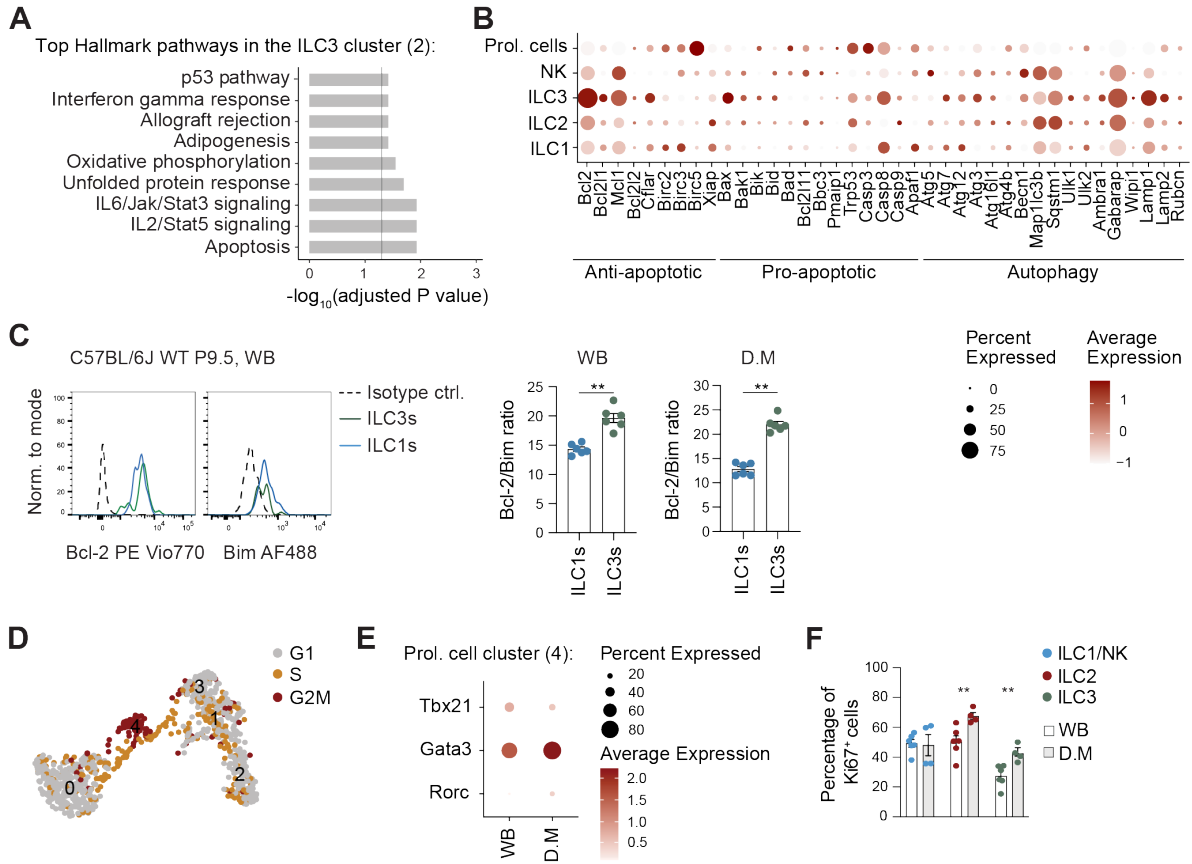
1295

1296

1297

1298

1299 **Figure 5**



1300

1301

1302

1303

1304

1305

1306

1307

1308

1309

1310

1311

1312

1313

1314

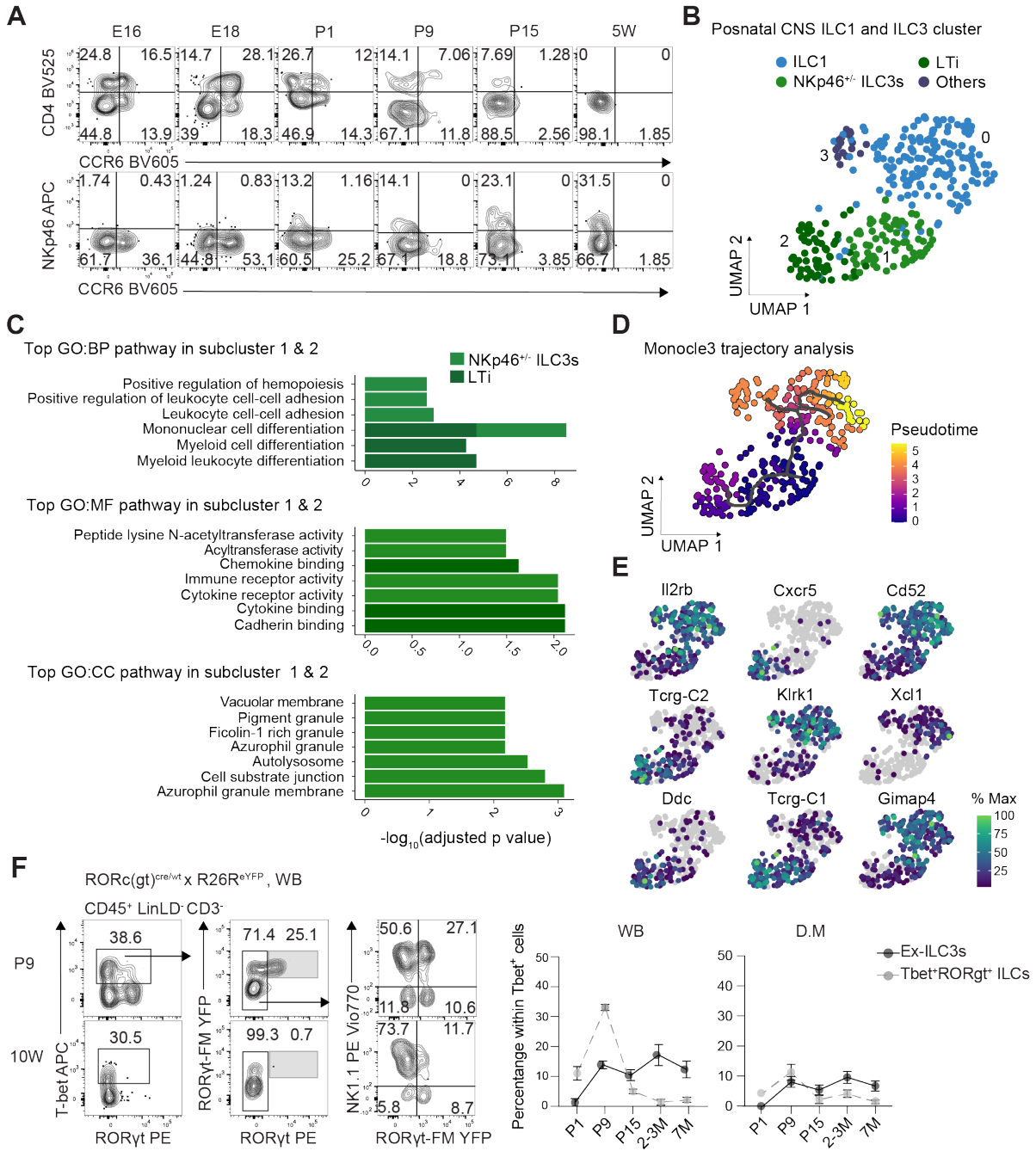
1315

1316

1317

1318

1319 Figure 6



1320

1321

1322

1323

1324

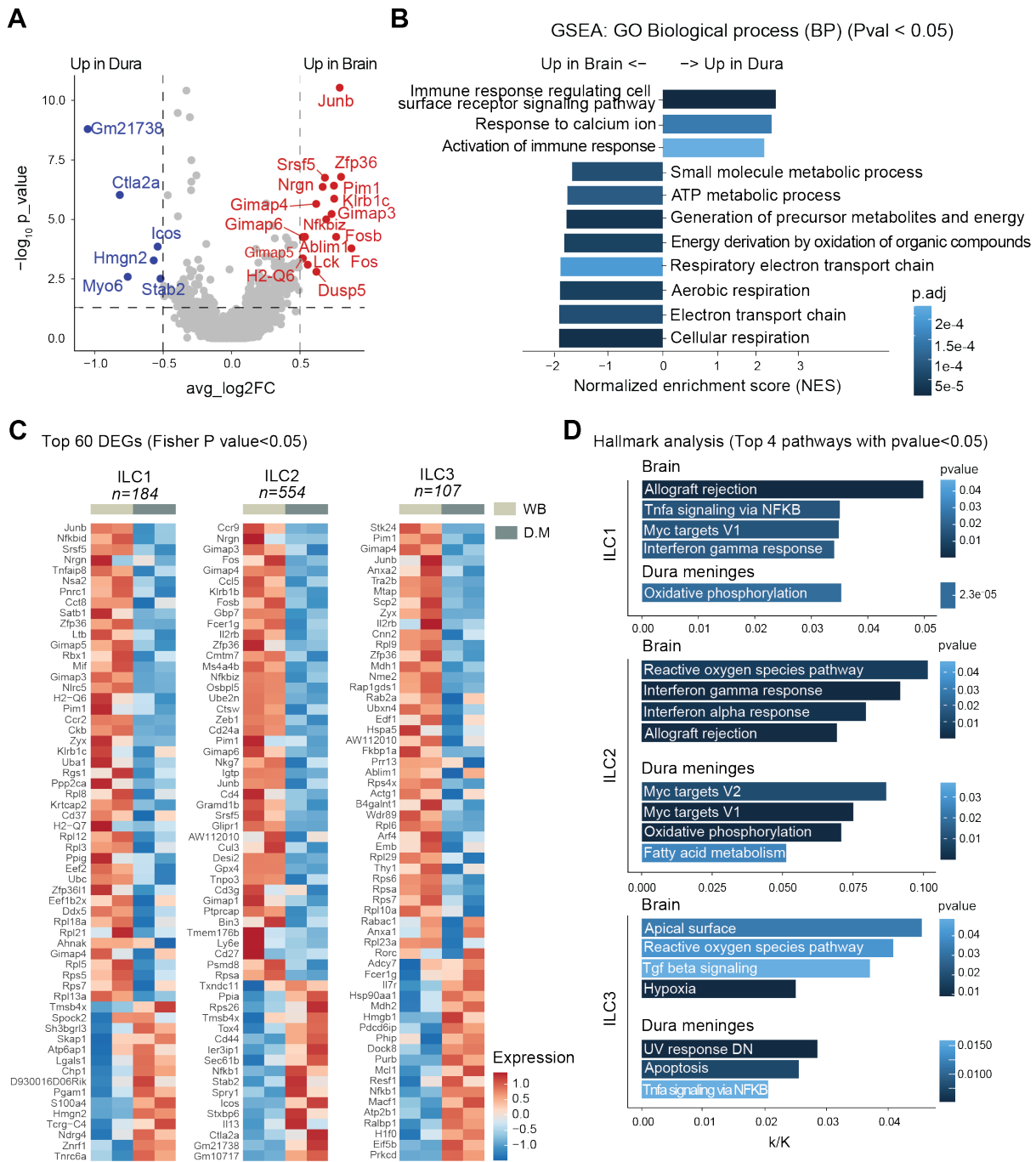
1325

1326

1327

1328

1329 Figure 7



1330

1331

1332

1333

1334

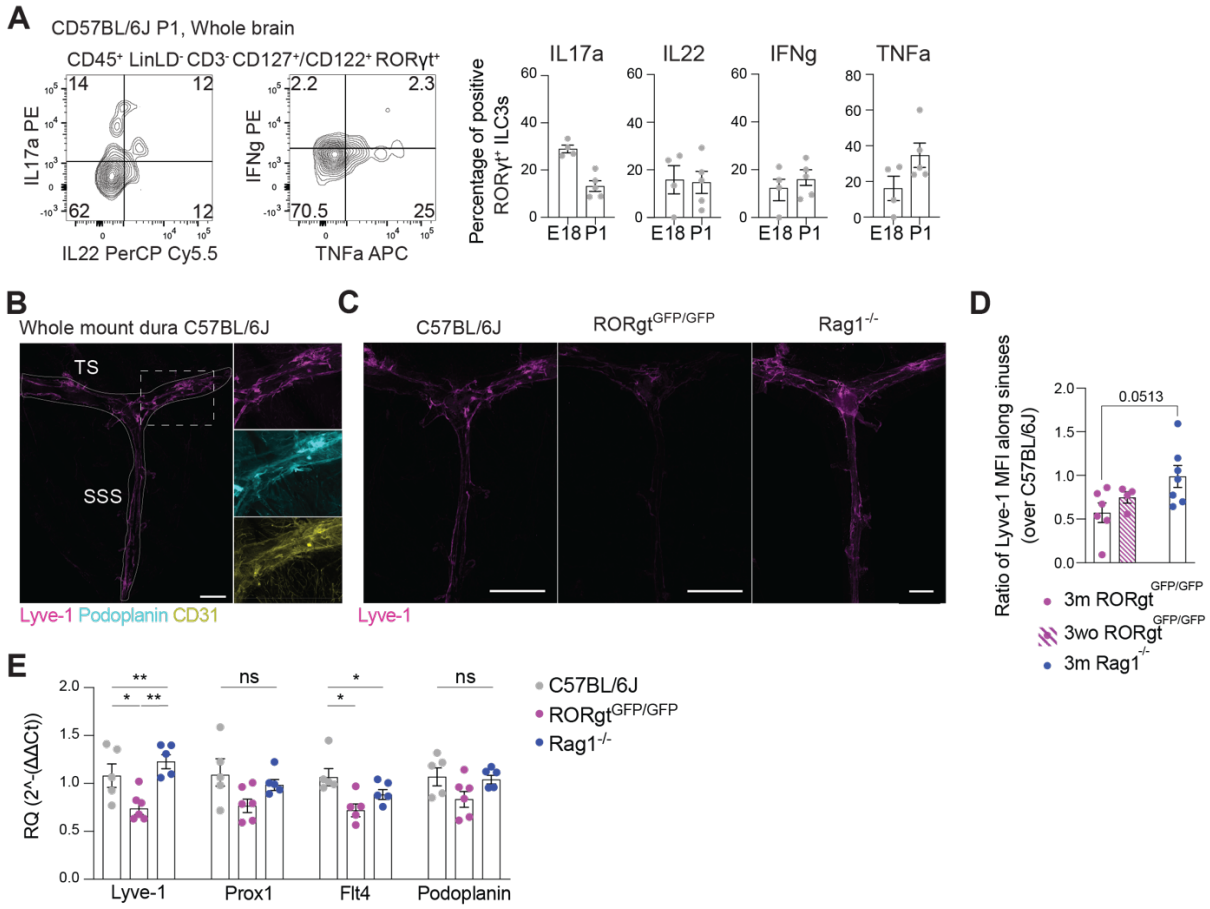
1335

1336

1337

1338

1339 Figure 8



1340
1341
1342
1343
1344
1345
1346
1347
1348
1349
1350
1351
1352
1353
1354
1355
1356
1357